An Optical Smart Needle: Point-Of-Care Technologies for Integrated Needle Guidance using Optical Frequency Domain Ranging

by

Brian David Goldberg

B.S., Electrical Engineering, Massachusetts Institute of Technology (2002)
B.S., Physics, Massachusetts Institute of Technology (2003)
M.Eng., Electrical Engineering, Massachusetts Institute of Technology (2003)

Submitted to the Harvard-MIT Division of Health Sciences and Technology
in partial fulfillment of the requirements for the degree of

Doctor of Philosophy in Medical and Electrical Engineering

at the

MASSACHUSETTS INSTITUTE OF TECHNOLOGY

September 2009

ARCHIVES

MASSACHUSETTS INSTITUTE OF TECHNOLOGY
OCT 0 2 2009
LIBRARIES

© Massachusetts Institute of Technology 2009. All rights reserved.

Author ....
Harvard-MIT Division of Health Sciences and Technology
July 31, 2009

Certified by ....
Guillermo J. Tearney, MD,PhD
Associate Professor of Pathology, Harvard Medical School
Thesis Supervisor

Accepted by ....
Ram Sasisekharan, PhD
Director, Harvard-MIT Division of Health Sciences and Technology
Edward Hood Taplin Professor of Health Sciences & Technology
and Biological Engineering

An Optical Smart Needle: Point-Of-Care Technologies for Integrated Needle Guidance using Optical Frequency Domain Ranging

by

Brian David Goldberg

Submitted to the Harvard-MIT Division of Health Sciences and Technology
on July 31, 2009, in partial fulfillment of the
requirements for the degree of
Doctor of Philosophy in Medical and Electrical Engineering

Abstract

Obtaining accurate needle placement is of critical importance in many medical scenarios. In the setting of fine needle aspiration biopsy (FNAB), manual palpation is often the only cue for determining the optimal position of the needle. As a result, FNAB procedures frequently yield non-diagnostic tissue. When not guided by an imaging modality, breast and thyroid FNAB's only obtain diagnostic tissue in approximately 65% of cases. Although the addition of noninvasive imaging technology has been shown to increase FNAB yield, it is time-consuming, relatively expensive, and often requires additional personnel with specialized expertise. A need exists for low-cost, small, simple to use technologies that can provide active feedback during needle placement.

One promising method for guiding needle placement would be to integrate an optical sensor that could identify tissue type at the tip of the needle in order to avoid non]diagnostic sampling. Optical technologies are well suited to this challenge because sensors can be made using optical fiber which is as thin a human hair. Optical frequency domain ranging (OFDR) is an optical ranging technique that is capable of measuring depth-resolved (axial, z) tissue structure, birefringence, flow (Doppler shift), and spectra at a micrometer level resolution. Analysis of the OFDR depth reflectivity profiles yields information about the nature of the tissue being interrogated at the tip of the probe and algorithms can be developed to automatically differentiate between tissue types.

The overall goal of this thesis is to develop a small, portable, point-of-care optical system that can be used to differentiate human breast tissue and guide needle placement in the setting of FNAB. We will investigate enabling technologies that allow for efficient simplification and miniaturization of an OFDR system including signal processing algorithms for automatically differentiating tissue type, a miniature battery-powered laser, and a study of the effect of reduced-bit depth acquisition for OFDR systems. Throughout, we will focus on trade offs between size and performance while taking into account usability, robustness, and overall cost which are key features of point-of-care technologies.

Thesis Supervisor: Guillermo J. Tearney, MD,PhD
Title: Associate Professor of Pathology, Harvard Medical School

Acknowledgments

I would like to thank my advisors, Drs. Gary Tearney and Brett Bouma, for their overwhelming support over the last several years. This work could not have been done without their mentoring and technical expertise for which I will be forever grateful. When I originally joined their lab as a summer student, I was naive to the fields of biomedical optics and clinical medicine. Through my experiences in HST, within the Wellman Center for Photomedicine, and my training in the lab, I have grown as a scientist and a person, and, hopefully, contributed to this growing field.

There are several current and former members of the Wellman Optical Diagnostics Group that deserve special mention. Dr. Nicusor Iftimia was the original project lead on the Smart Needle project and I have always valued his guidance. Dr. Reza Motaghiannezam and Priyanka Jillella were members of the Smart Needle team during this thesis and I am grateful for their help. I would also like to mention Dr. Martha Pitman, our clinical collaborator, and Sven Holder, both a huge help and a friend in the Pathology department.

Dr. Ben Vakoc and Dr. William Oh have been a continued resource for technical help and thoughtful discussions regarding OFDI and laser design. Dr. Alyx Chau was my office mate and fellow graduate student throughout my PhD years. I like to think we navigated the PhD waters together and am happy we both accomplished our goals. Alyx was also a huge resource for software and MATLAB help as well as a sounding board for new ideas, life, and the lab. Other people who have given me great help over the years include Jason Bressner, Dr. Melissa Suter, Dr. Milen Shishkov, Dr. Semantini Nadkarni, Dr. Adrien Dejardins, Dr. Caroline Boudoux, Dr. Hyle Park, Dr. Conor Evans, Dr. Aydogan Ozcan, Dr. Alberto Bilenca, Dr. Dongkyn Kang, and Dr. Max Colice. Of special mention is Dr. Ray Chan, who has been a friend, colleague, and mentor since I started in this field. Ray encouraged me to apply to HST and has been a continued resource in science and in life for many years. I highly value our continued friendship.

I would like to thank my family and friends for giving me the emotional support needed to complete my PhD. A PhD can sometimes be a long and challenging road, and without their support I never would have finished. My parents, Wendy and Hal, have been a continued source of love and support, and my brother, Michael, has been a great friend since we were kids. I only wish that we could be together more often. I would also like to thank my in-laws, Joe and Kristie, for their support of Joanna and me and their help navigating the PhD path.

The most important person in my PhD journey has been my wife and best friend, Joanna. She continued to believe in me, pushed me, and sacrificed for me. She was patient, loving, and kind. I always found encouragement knowing she was right there beside me. Last, but not least, the best reward of all has been the arrival of our first child, Daniel. Daniel, you have been a source of immense joy and love for our entire family. May you, and our entire family, continue to find love and support in each other in the years ahead.

Contents

1 Introduction **17**

1.1 Motivation . . . 18

1.1.1 Point-of-Care Technologies . . . 18

1.2 Fine Needle Aspiration Breast Biopsy . . . 19

1.2.1 Needle Guidance . . . 20

1.3 Thesis Summary . . . 21

1.3.1 Thesis Outline . . . 22

2 Low Coherence Interferometry and Optical Frequency Domain Ranging **25**

2.1 POC Design Criteria . . . 25

2.2 Optical Coherence Tomography . . . 26

2.3 Low Coherence Interferometry . . . 27

2.3.1 Theory . . . 27

2.3.2 Noise . . . 30

2.3.3 Benchtop System . . . 32

2.4 Optical Frequency Domain Ranging . . . 35

2.4.1 Theory . . . 36

2.4.2 Noise . . . 37

2.5 Summary 39

3 **Automated Algorithm for Human Breast Tissue Differentiation** **41**

3.1 Introduction 41
3.2 *In-vitro* Study 42
  3.2.1 Experimental Design 43
  3.2.2 Parameter Extraction 45
  3.2.3 Algorithm Model 48
  3.2.4 Intra-sample Variability 49
  3.2.5 Statistical Analysis 49
  3.2.6 Results 50
  3.2.7 Training Set 51
  3.2.8 Validation Set 52
  3.2.9 Intra-sample Variability 56
3.3 Discussion 56

4 **Miniature Swept Source** **59**

4.1 Introduction 59
4.2 Experimental Setup 60
  4.2.1 Laser Design 60
  4.2.2 OFDI imaging setup 63
4.3 Results 63
  4.3.1 Laser characteristics 63
  4.3.2 Battery powered operation 67
  4.3.3 OFDI Imaging 67

4.3.4 Comparison of LCI and OFDR 69
4.4 Discussion 70
4.5 Summary 73

5 Reduced Bit-Depth Data Acquisition 75

5.1 Introduction and Motivation 75
5.2 Principles 78
5.3 Noise analysis 79
5.3.1 OFDI noise 79
5.3.2 Quantization noise 80
5.4 Experiments 81
5.4.1 OFDI System 81
5.4.2 Noise measurements 82
5.4.3 Bit-depth reduction 85
5.5 *In vivo* imaging 88
5.6 Implications for OFDI 89

6 Discussion 95

6.1 POC Design Criteria 95
6.1.1 Automated Algorithm 95
6.1.2 Miniature Source 96
6.1.3 Reduced Bit-Depth Acquisition 97
6.1.4 Additional Design Elements 99
6.2 Summary and Conclusion 105

THIS PAGE INTENTIONALLY LEFT BLANK

List of Figures

2-1 Schematic of low coherence interferometry. 28

2-2 Photograph of the LCI biopsy guidance instrument 32

2-3 Photograph of the FNAB LCI probe. 33

2-4 Schematic of the LCI biopsy guidance instrument. 34

2-5 OFDI Schematic 35

3-1 FNA gun mounted with needle and positioned above sample. 44

3-2 Average powre spectrum data from LCI depth scans. 48

3-3 Characteristic axial depth scans from adipose and fibroglandular human breast tissue. 50

3-4 Scatter plot representation of training set data. 53

4-1 Miniature wavelength-swept laser source schematic. 61

4-2 OFDI Imaging setup. 64

4-3 Laser trace showing ~2.5 full sweeps of the resonant scanner. 65

4-4 Tuning bandwidth, shown in log scale. 66

4-5 Characteristic fringe pattern from a fixed reflector. 67

4-6 Axial point-spread function from a fixed reflector for forward and backward sweeps. 68

4-7 Signal roll-off as a function of depth for the forward and backward wavelength sweeps. 68

4-8 Laser output power as a function of time on full battery power. 69

4-9 5 mm x 2.25 mm OFDI images from the ventral surface of a human forefinger. Forward (left), backward (middle), and combined (right) wavelength sweep images. 69

4-10 Comparison of LCI and OFDR depth reflectivity profiles. 70

5-1 OFDI system schematic. 82

5-2 DAQ and DAQ plus thermal noise measurements at 3,1.6, and 1V V_{max}. . . 83

5-3 Shot plus RIN noise as a function of reference arm power. 84

5-4 SNR as a function of bit-depth from 6 to 14 bits at four sample arm attenuation levels (44.3, 65.8, 75.2, 86.6 dB) and a 1V V_{max}. 87

5-5 Change in SNR as a function of bit-depth. 88

5-6 Images from a human coronary acquired *in vivo* showing a calcific nodule (arrow). 90

5-7 Images from a human coronary acquired *in vivo* showing a highly reflective metal stent. 91

6-1 Integrated optical fiber/needle probe design where optical fiber travel travels within a separate lumen. 100

6-2 Integrated optical fiber/needle probe design with optical fiber protected within a hypodermic tube. 102

6-3 Integrated optical fiber/needle probe design with optical fiber protected within a hypodermic tube and offset from needle tip to avoid cutting edge. 102

6-4 Integrated optical fiber/needle probe design with double lumen for aspirate and optical fiber. 103

6-5 Integrated optical fiber/needle probe design with optical fiber attached to the side, top, or bottom of the needle. 104

6-6 Integrated optical fiber/needle probe design with optical fiber running in a groove of the FNA needle. 104

THIS PAGE INTENTIONALLY LEFT BLANK

List of Tables

3.1 Training set statistics 52

3.2 Validation set statistics 54

3.3 Classification results for 3-parameter model. 55

3.4 Classification results for 2-parameter model. 55

3.5 Model comparison. 55

6.1 DAQ design criteria for POC FNAB guidance. 99

THIS PAGE INTENTIONALLY LEFT BLANK

Chapter 1

Introduction

The overall goal of this thesis is to investigate the use of low coherence interferometry (LCI), and its second generation form optical frequency domain ranging (OFDR), for integrated guidance of fine needle aspiration biopsy (FNAB) procedures and to develop novel optical technologies that enable point-of-care (POC) implementation. While these technologies will be useful in a number of clinical settings, this thesis will focus on FNAB guidance for breast cancer detection. We will investigate enabling technologies that allow for efficient simplification and miniaturization of an OFDR system including signal processing algorithms for automatically differentiating human breast tissue types, development of a miniature laser, and reduced bit-depth acquisition of the OFDR signal. Throughout the thesis we will focus on trade offs between size and performance while taking into account usability, robustness, and overall cost, which are key features of POC technologies.

1.1 Motivation

1.1.1 Point-of-Care Technologies

POC technologies aim to bring advances in medical technology directly to the patient. New POC technologies are emerging for performing bedside diagnostic imaging [1–3], obtaining lab chemistries [4–6], and improving information management [7–9]. In 2006, the NIH held a symposium entitled "Improving Health Care Accessibility Through Point-of-Care Technologies" under the hypothesis that performing tests "closer to the point of care may reduce fragmentation of care and improve outcomes" [10]. A successful POC technology must be small, inexpensive, lightweight, accurate, robust, and easy to use. In many respects, the concept of POC diagnostics is not new. Before the advent of advanced clinical tests and imaging studies, almost all medical observation and diagnostics were done at the patient's bedside. Today, many of these tests are performed through central labs within hospitals. However, POC testing, imaging and diagnostics are becoming more and more common within many medical settings including primary, home, and emergency care [10].

Imaging has the potential to play a key role within the field of new POC technologies. Imaging allows the physician to see deeper, with higher resolution, and with greater contrast than with the naked eye. At the point of care, imaging can provide crucial diagnostic information [11], guide procedures [12], and identify tumor margins during surgical biopsies [13]. In other settings, new imaging technologies are performing comprehensive screening in ways that may eliminate the need for biopsies altogether [14–16].

1.2 Fine Needle Aspiration Breast Biopsy

FNAB is often the first line of diagnosis for a palpable mass [17–19]. In order to perform an FNAB, the mass is manually stabilized, a small diameter needle (typically 23 or 25 gauge) is inserted into the mass, and a small amount of tissue or fluid is aspirated into the needle. The aspirate within the bore of the needle is then expressed onto a slide, smeared, stained, and examined by a pathologist. Due to the small size of the needle, patient discomfort is generally limited to the initial stick of the needle. Complications including hematoma and infection are rare [20, 21]. The simplicity of FNAB significantly reduces the time and cost of obtaining an initial diagnosis compared with core or excisional tissue biopsy and allows rapid feedback to both the clinician and patient. In addition, comparisons of the sensitivities and specificities of core needle biopsy (CNB) and FNAB for palpable masses show them to be high and similar [21, 22]. As a result, FNAB has become a frequently utilized diagnostic tool for the evaluation of many superficial, palpable masses.

Manual palpation of a superficial mass is often the only cue for determining the optimal position of the needle in tissue during biopsy. As a result, FNAB can frequently be non-diagnostic, especially with an inexperienced operator [23–27]. Sample adequacy is graded on a sliding scale based on the degree of epithelial cellularity from which a diagnosis can be made [26, 27]. Non-diagnostic samples are completely void of epithelial cells and consist primarily of adipose cells and cyst fluid [27]. When not guided by an imaging modality, breast FNAB's obtain diagnostic tissue in approximately 65% -78% of cases [23,25,26]. This is particularly problematic when performing FNAB's in locations that are rich in adipose tissue, such as the breast and axilla. One method of increasing FNAB yield is concomitant use of non-invasive imaging devices, such as ultrasound, to guide needle placement. Radiologic guidance is almost always employed when FNAB is performed on non-palpable masses.

While the addition of non-invasive imaging technology has been shown to increase FNAB yield, it is time consuming, relatively expensive, and often requires additional personnel with specialized expertise [20]. A need exists for POC needle guidance technologies in the setting of FNAB that fit the criteria established by the NIH. For these reasons we chose to focus on the development of miniature OFDR systems for POC FNAB needle guidance solutions.

1.2.1 Needle Guidance

Imaging is already playing a role in needle guidance. MR, CT, and ultrasound guided needle biopsies are used to access lesions in the head and neck [12], lung [28], and breast [20] as well as for obtaining vascular access [29]. However, these technologies are often large, expensive, require additional personnel to operate, and are not available in all clinical settings. Optical technologies are well suited for POC needle guidance because sensors can be made using optical fibers which are as thin a human hair. Other groups have investigated the use of needle based optical probes for biopsy guidance based on imaging [30], or by direct measure of tissue optical properties such as multispectral reflection analysis [31], scattering coefficient [32], or refractive index [33] measurements. Miniature optical needle probes have also been utilized to correlate brain motion with ECG waves in a minimally invasive fashion [34].

One promising method for guiding needle placement is the use of coherence gating techniques such as LCI [35], and its second generation form OFDR [36]. LCI and OFDR are optical ranging techniques capable of measuring depth-resolved (axial, z) tissue structure, birefringence, flow (Doppler shift), and spectra at a micrometer-level resolution. Analysis of the depth reflectivity profiles yields information about the nature of the tissue being interrogated at the tip of the probe and algorithms can be developed to automatically differentiate between tissue types. In medical imaging, OFDR is often known as the one-dimensional building block of Optical Frequency Domain Imaging (OFDI) [36]. These techniques have advantages over point sampling techniques such as spectroscopic analysis or refractive index measurements because they provide a depth-resolved reflectivity profile that provides information as to tissue structure. High resolution tissue boundaries can be determined with OFDR because the axial resolution is on the order of a few microns.

The simplest and smallest probe in an OFDR system is a single optical fiber which can be as small as 80 µm in diameter. Standard 23 and 25 gauge FNAB needles have inner diameters of 330 and 250 µm respectively. Therefore, a single optical fiber with no additional distal optics takes up 5-10% of the needle lumen area. It is theoretically possible to turn an OFDR needle guidance system into an OFDI imaging system by placing distal focusing optics onto the fiber probe and spinning the fiber to produce a forward looking arc or side-viewing circumferential image. However, additional optics may interfere with the FNAB aspirate collection because they take up larger percentages of the needle lumen and the mechanical mechanisms needed to spin the fiber add cost, bulk, and complexity to the POC technology.

1.3 Thesis Summary

In this thesis we will develop technologies to miniaturize and simplify an OFDR system capable of guiding needle placement with an emphasis on guiding FNA breast biopsies. Although we will focus on the application of FNA breast biopsy, the concept of POC integrated needle guidance can have a broad reaching clinical impact. Our approach includes the development of a new, miniature, battery powered swept-laser that's capable of delivering enough power and resolution for obtaining adequate OFDR signals. Although we will not directly work on the miniaturization of the detector and computer components, as this is outside the scope of this thesis, we will study the use of reduced bit-depth acquisition which is important for reducing the size of current data acquisition systems. Reduced bit-depth detection schemes can maintain imaging speeds while reducing data storage needs. In the setting of FNA breast biopsies, we will also develop algorithms to differentiate tissue types.

1.3.1 Thesis Outline

The thesis will begin with the theory of both LCI and OFDR along with a discussion of their benefits and limitations. Chapter 2 will also include a discussion of the system specifications required for making a useful POC technology. Prior to this thesis, a bench top LCI needle guidance system was developed in our lab and used to demonstrate the concept of integrated optical needle guidance for FNAB [37]. The system was optimized and used in an *ex vivo* study as part of this thesis. A brief description of the LCI system will be presented in chapter 2.

An *ex vivo* study of excised human breast tissue samples will be discussed in chapter 3. This study further tested the ability of LCI to differentiate human breast tissue type. An automated algorithm for classifying adipose and fibroglandular breast tissues was developed and the sensitivity and specificity of the model was determined prospectively in a blinded fashion. Intra-sample variability of the algorithm was also tested to assess the robustness of the algorithm. The algorithm was an important step in making optical guidance of FNAB more suitable for real-time clinical use by making the tissue classification automatic without any user input.

The LCI system used for the *ex vivo* studies is about the size of a briefcase and not suitable for hand-held clinical use, a necessity for POC FNAB guidance. Chapters 4 and 5 discuss enabling technologies for making a truly hand-held optical needle guidance system. Chapter 4 presents a novel miniature wavelength-swept laser suitable for POC OFDR. The system can be fully battery powered, has a small footprint, and achieves peak power and tuning speeds approaching current swept sources used in clinical OFDI systems.

One challenge in making a miniature OFDR systems is that currently available data acquisition (DAQ) systems of sufficient speed are too large and do not fit within our desired form factor. It is common in OFDR to use DAQ boards with 12 or 14 bit resolution. At high speed data acquisition, these boards also present challenges with data transfer rates and data storage. The development of a truly miniature DAQ board is beyond the scope of this thesis. However, in chapter 5 we will study the use of reduced bit-depth data acquisition which is important for reducing the size of current data acquisition systems. Reduced bit-depth detection schemes can maintain imaging speeds while reducing data storage needs. This analysis extends beyond that of POC system development. The advancement of high speed OFDI presents similar challenges which can limit the practical imaging speed of clinical systems. Chapter 6 will also include a discussion of the sampling requirements for a POC needle guidance system in the light of reduced bit-depth acquisition schemes.

The thesis will conclude with a summary of the work. The thesis contains enabling technologies for a POC OFDR system. The next phase of this work is to incorporate the different technologies into a fully packaged, hand-held, POC needle guidance system and to test the algorithm in an *in vivo* setting.

THIS PAGE INTENTIONALLY LEFT BLANK

Chapter 2

Low Coherence Interferometry and Optical Frequency Domain Ranging

2.1 POC Design Criteria

As discussed in chapter 1, a successful point-of-care (POC) technology must be small, inexpensive, lightweight, accurate, robust, and easy to use. In addition, a technology that seamlessly integrates with the current standard of care practice will be more easily accepted by the medical community. In the setting of fine needle aspiration biopsy (FNAB), the current procedure only requires a small needle and a biopsy gun (see Fig. 3-1). The procedure is usually done in a small office or procedure room and the clinician requires 360 degree access around the patient in order to position the biopsy needle from a variety of angles. An FNAB procedure usually lasts only 10-15 minutes and 3 to 5 separate biopsies are obtained [38]. A large scale guidance technology that restricts the clinician's movement would negatively impact the performance of FNAB procedures and reduce its acceptance within the medical community.

With this in mind, we set out to design and build a small, portable, and inexpensive POC needle guidance system that could be used to improve FNAB yield and reduce non-diagnostic sampling. Our goal was to build an entire system for under \$10,000 with optical probes that fit directly into standard FNAB needles. Ideally, the system would be small and portable enough to be hand-held or worn on a physician's belt such that the guidance system would not restrict the physician's movement in any way. The system would automatically perform signal analysis without requiring any additional input required from the physician and be fast enough to reduce motion artifacts caused by physician or patient movement. In addition, although the simplest system design uses only one-dimensional signals, a system of sufficient speed could in principle generate two and three-dimensional images at video-rate.

2.2 Optical Coherence Tomography

In the past decade, optical coherence tomography (OCT) has emerged as a powerful medical imaging technology for obtaining cross-sectional images of biological tissue. OCT is capable of measuring depth-resolved reflectivity profiles with axial resolutions in the 5-10 μm range. By scanning the image beam or moving the sample, the depth reflectivity profiles can be stacked together to create a tomographic image. Therefore, these images are often referred to as an "optical biopsy" and resemble histologic sections obtained by standard biopsy and staining techniques. OCT was first introduced in 1991 by Huang et. al [35]. The original design, now referred to as time-domain OCT (TD-OCT) is based on low coherence interferometry (LCI), which uses a broadband laser source, and a Michelson interferometer with a moving reference arm to achieve depth sectioning. TD-OCT is analogous to ultrasound with laser light in that a laser source illuminates the sample, and time-of-flight data is encoded interferometrically, thereby achieving a depth-resolved reflectance signal.

OCT has been used in a wide array of clinical applications including opthalmology, cardiology, gastroenterology, and breast pathology [39]. Imaging speed limitations of TD-OCT led investigators to invent second generation OCT technologies. These systems, known as Fourier domain OCT (FD-OCT), can achieve faster imaging speeds as well as improved signal to noise ratios (SNR) compared with TD-OCT. These improvements have enabled FD-OCT to achieve *in-vivo* 3D volumetric imaging in the esophagus and coronary arteries [40–42].

The following chapter will include a treatment of the theory of LCI as well as FD-OCT in one of its implementations known as optical frequency domain imaging (OFDI), also known as swept-source OCT (SS-OCT). The one dimensional building block of OFDI is known as optical frequency domain ranging (OFDR). In addition, an LCI system designed for guiding needle placement will be described. This system was optimized and used in an *ex-vivo* tissue classification study described in chapter 3.

2.3 Low Coherence Interferometry

2.3.1 Theory

Low coherence interferometry is an optical ranging technique that achieves depth sectioning on the order of a few microns. In its simplest form, LCI uses a broadband light source and a Michelson interferometer (Fig. 2-1). The broadband, low-coherence, light source is directed into a Michelson interferometer and split into sample and reference arms. In the TD-OCT configuration, the reference arm path length is varied mechanically over a range of 2-3 mm, keeping the sample arm path length constant.

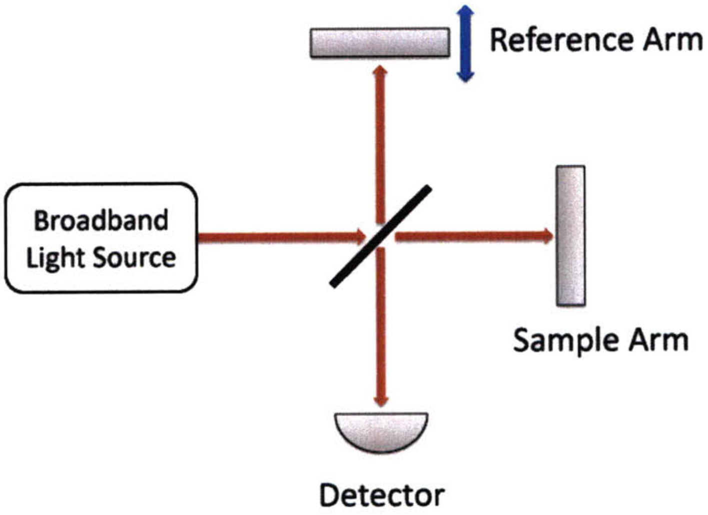

Figure 2-1: Schematic of low coherence interferometry.

At the detector, the time-averaged signal current can be written as

$$\mathrm{I} = \frac{\eta e}{h\nu}\left(\frac{1}{\eta_0}\right)\left[\left|E_{r0}\right|^2 + \left|E_{s0}\right|^2 + \mathrm{real}\left\{E_s E_r^*\right\}\right], \tag{2.1}$$

where η is the detector quantum efficiency, e the electric charge, h Plank's constant, ν the optical frequency, and η_0 is impedance of free space. The first two terms represent the DC power from the reference and sample arms respectively and the last term is the cross-correlation between the two arms. The last term generates an AC signal and can be expanded as,

$$\mathrm{real}\left\{E_r E_s^*\right\} \quad = \quad E_{r0} e^{-j(2\beta_r(\omega) l_r - \omega t)} * E_{s0} e^{j(2\beta_s(\omega) l_s - \omega t)} \tag{2.2}$$

where l_r and l_s are the optical path lengths for the reference and sample arms and $\beta_{r/s}(\omega)$ is the propogation constant as a function of wavelength given by $\beta = 2\pi/\lambda$. For a broadband source, the total signal current is the integration of Eq. 2.2 across the spectral bandwidth. The AC signal then becomes

$$\mathrm{I_{ac}} \quad \propto \quad \int E_{r0} e^{-j(2\beta_r(\omega) l_r)} * E_{s0} e^{j(2\beta_s(\omega) l_s)} \frac{d\omega}{2\pi}. \tag{2.3}$$

By assuming $\beta_r = \beta_s = \beta$ and expanding $\beta(\omega)$ around the center frequency we can write

$$\beta(\omega) = \beta_0(\omega_0) + \beta'(\omega - \omega_0) \tag{2.4}$$

and then

$$\mathrm{I_{ac}} \quad \propto \quad e^{-j(2\beta_0 \Delta l)} \int E_{r0}(\omega) E_{s0}(\omega) e^{-j(2\beta'(\omega-\omega_0)\Delta l)} \frac{d\omega}{2\pi}. \tag{2.5}$$

$\mathrm{I_{ac}}$ as a function of pathlength difference, Δl, has a carrier frequency determined by the phase velocity of the laser source. Assuming equal amplitudes for E_{r0} and E_{s0}, $E_{r0}E_{s0}^*$ is the power spectral density of the source and the integral term of equation 2.5 is its Fourier transform. Therefore, the AC signal term consists of a carrier frequency and an envelope function which is the Fourier transform of the source shape.

In an ideal LCI system the sample arm is linearly scanned, and, for a fixed reflector in the sample arm, $l_s = z_0$, the pathlength difference becomes a periodic function given by

$$\Delta l(t) = v * (t - nT), n = 0, 1, 2, 3, \ldots \tag{2.6}$$

where v is the velocity and T the period of the reference arm scanner. Therefore, the real part of I_{ac} becomes

$$I_{ac} \propto \cos(2\beta_0 vt) * G(\tau) \tag{2.7}$$

where $G(\tau)$ is the coherence function of the laser source, given by the Fourier transform of the source spectral density. The coherence function defines the axial resolution because as the reference arm is scanned, only near the position where $\Delta l = 0$ is there appreciable signal. The carrier frequency is given by $f_c = \beta_0 v/\pi$ and the coherence function depends on the source spectral width. It is well known that Fourier transform pairs have an uncertainty relationship such that a broader source shape produces a tighter coherence function. The coherence function is often defined in terms of its coherence length. Several definitions exist within the literature, but the most common is given by

$$l_c \approx 0.44\frac{\lambda_0^2}{\Delta\lambda} \tag{2.8}$$

where $\Delta\lambda$ is the source width in wavelength [43] and the spectral shape is Gaussian.

In biological samples, the sample arm contains at different depths, and the coherence function provides the depth sectioning by limiting the signal from a particular Δl to within the coherence length. Signal detection and demodulation in LCI occurs by first digitizing the signal, band pass filtering, and then frequency shifting the signal about the carrier frequency. The resulting signal represents the depth-resolved (axial z) reflectivity profile of the sample arm.

2.3.2 Noise

The main noise terms in LCI, or TD-OCT, are thermal, shot, and relative intensity (RIN) noise. Thermal noise comes from the detection electronics and is independent of the optical power. Shot noise arises from the fact that individual photons reach the detector at random times, and not in a continuous stream. This produces fluxuations in the number of photons that reach the detector for any one time-interval. The noise associated with this variation is linearly related to the optical power and given by

$$\sigma_{shot}^2 = 2e\frac{\eta e}{h\nu}(P_{ref} + P_{sam}) \tag{2.9}$$

where P_{ref} and P_{sam} are the reference and sample arm powers respectively. RIN noise arises from fluxuations in the source power and is related to the square of the optical power.

$$\sigma_{RIN}^2 = \frac{\eta e}{h\nu}^2 \tau_{coh}(P_{ref} + P_{sam})^2 \tag{2.10}$$

Here, τ_{coh} is a parameter that defines the coherence time of the laser [44]. In LCI for biological applications, the reference arm power is set such that $P_{ref} >> P_{sam}$. The total noise is given by the individual noise terms multiplied by the detection bandwidth given by $NEB = \Delta\lambda f_c/\lambda_0$. The signal power in LCI is given by

$$SignalPower = 2 * \frac{\eta e}{h\nu}^2 P_{ref} * P_{sam}. \tag{2.11}$$

Thus, if the shot noise dominates over the RIN noise, the SNR is given by

$$SNR_{LCI} = \left(\frac{\eta}{h\nu}\right)\frac{P_{sam}}{NEB}. \tag{2.12}$$

2.3.3 Benchtop System

Chapter 1 introduced the concept of needle guidance using optical imaging technologies. Prior to this thesis, a benchtop LCI system was developed with the goal of building a portable system for fine needle aspiration biopsy (FNAB) guidance [37]. The system was designed to be low cost, portable, simple to use, with probes that could easily be integrated with standard FNAB needles. All the optical and electronic components fit within a briefcase sized housing as shown in Fig. 2-2. The sample arm probe, which was integrated directly into a standard FNAB needle, is shown in Fig. 2-3 and consisted of a single mode optical fiber that was angle cleaved and positioned at the tip of the biopsy needle. This simple design produced a forward looking probe that interrogated the tissue directly in front of the needle tip.

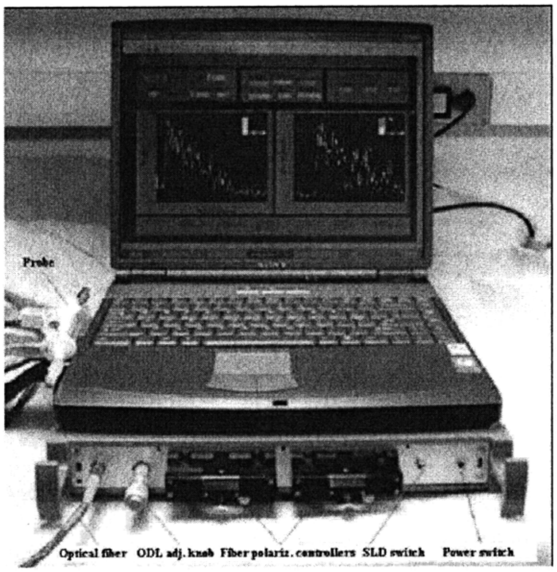

Figure 2-2: Photograph of the biopsy guidance instrument taken from [37].

A full system schematic is shown in Fig. 2-4. A broadband super-luminescent diode (SLD) centered at 1310 nm with a full width at half maximum bandwidth of 50 nm (Optiphase, Inc., Van Nuys, California) was used as a light source. Therefore, the axial resolu-

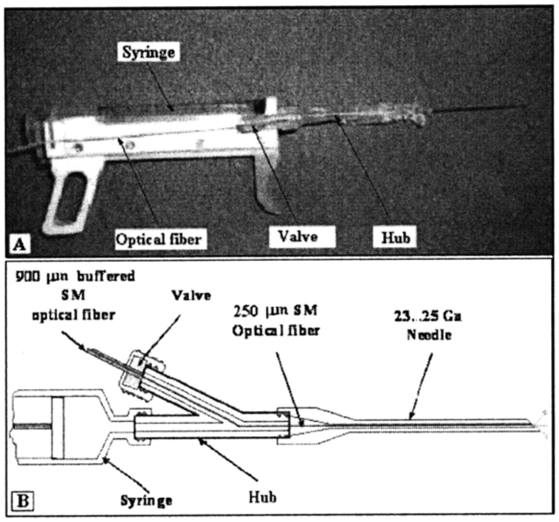

Figure 2-3: Photograph of the FNAB LCI probe taken from [37].

tion as determined by the coherence length was ~ 15 μm in air, or 11 μm in tissue (n=1.4). The source was directed through a fiber optic circulator and then into a a nonreciprocal fiber optic Michelson interferometer. The reference arm optical delay line (ODL) consisted of a retroreflector mounted on a galvanometer-driven lever arm which was scanned over a range of 1.5 mm at 20 Hz. The sample arm consisted of the fiber optic probe shown in Fig. 2-3. Approximately 750 μW was directed into the sample arm probe and onto the sample. At near shot noise limited detection, the maximum ahieved sensitivity was 101 dB. The detection arm consisted of a polarization beam splitter (PBS) and two detectors to achieve polarization-diverse detection. The detected signal was digitized and saved onto a computer for processing. The entire system was built for approximately $10,000.

In summary, the LCI system was a relatively small, low cost system which could achieve depth sectioning of 11 μm in tissue over a range of 1.5 mm. The system and optical needle probe were used to show the feasibility of differentiating human breast tissue types by demonstrating that the two main tissue types in the breast, adipose and fibroglandular tissue, had different axial-reflectivity profiles [37]. However, the sample size was small and

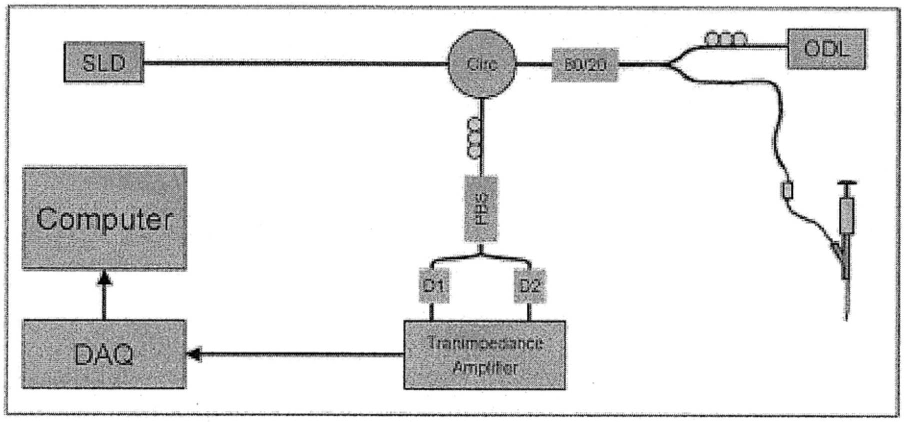

Figure 2-4: Schematic of the LCI biopsy guidance instrument. A super-luminescent diode (SLD) is sent through a circulator (Circ) and an 80/20 splitter. The LCI-FNA probe consists of a single mode fiber inserted through a hub connecting the syringe and the needle. An optical connector attaches the LCI-FNA probe to the sample arm of the interferometer.

the analysis was only semi-automated. Chapter 3 will discuss a larger scale *ex vivo* study performed with the LCI system for automatically measuring and differentiating these tissue types.

Due to the relatively slow scan speed of only 20 Hz, the LCI system was susceptible to motion artifacts due to probe or sample movement. In addition, although relatively small, the briefcase sized system was not suitable for hand-held clinical use as is the goal for a POC needle guidance system. Therefore, a goal for a second generation system was to increase the imaging speed and decrease the form factor of the FNAB guidance system.

In theory, it is possible to scan the reference arm optical delay line in an LCI system to achieve faster imaging speeds. However, mechanical considerations place practical limitations on the A-line rates that can be achieved. In addition, as the A-line rate is increased, the NEB also increases and the SNR is decreased. Thus, there are both mechanical and SNR based reasons why LCI, or TD-OCT, technology cannot achieve the design criteria for a hand-held POC needle guidance system. The next section will discuss the development of one of the second generation of OCT technologies, OFDI, and its one-dimensional building block OFDR. OFDI/OFDR systems can achieve the necessary imaging speeds and SNR values that would allow for a small, low-cost, portable POC system for needle guidance.

2.4 Optical Frequency Domain Ranging

In OFDI/OFDR, instead of scanning the reference arm to produce depth scanning, a wavelength-swept source is used with a fixed reference arm (Fig. 2-5), and depth-sectioning is encoded in the Fourier domain. It has been shown that OFDI systems have a significant SNR gain over TD-OCT [36,44–46]. The ability to build very high speed wavelength swept lasers [47–49] and the SNR advantage enable OFDI to achieve video rate imaging speeds with large ranging depths, high sensitivity, and high axial resolution.

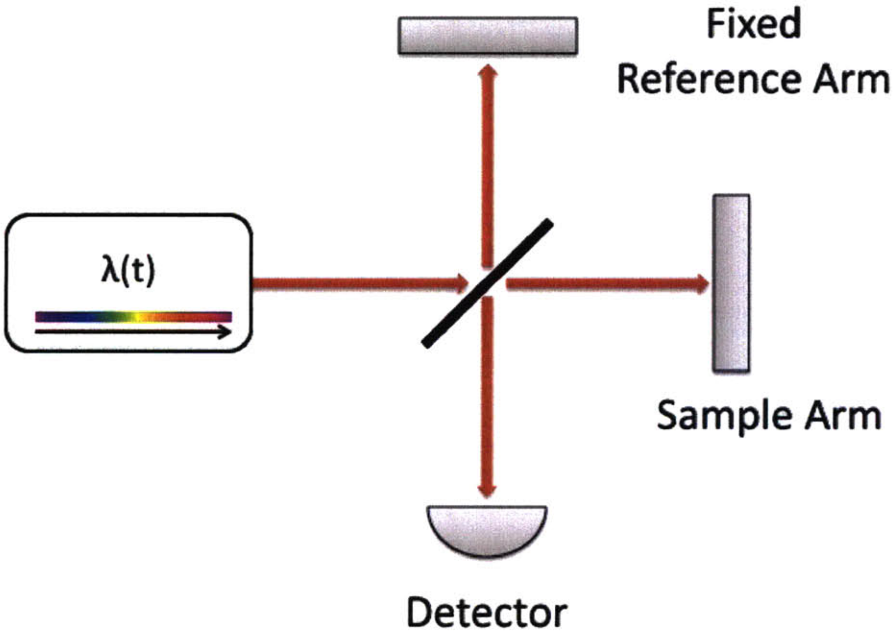

Figure 2-5: OFDI Schematic

2.4.1 Theory

For a fixed reflector in the sample arm, the photocurrent in OFDR can be expressed as

$$I(t) = \frac{\eta e}{h\nu}[P_{ref} + P_{sam} + 2 * \cos(2 * \frac{2\pi}{\lambda(t)}\Delta z)] \tag{2.13}$$

where $\lambda(t)$ represents the wavelength tuning of the wavelength swept source and Δz is the optical pathlength difference between the sample and reference arms. Just as in TD-OCT/LCI, the first two terms in Eq. 2.13 are the DC power terms from the sample and reference arms, and the last term is the AC signal that contains the frequency encoded pathlength difference. Alternatively, the last term can be written in term of the laser's wavenumber value $k = 2\pi/\lambda$. Therefore, the AC signal in OFDR is analogous to a sampling problem of a fixed frequency tone in the time-domain.

$$\cos(2k\Delta z) \longleftrightarrow \cos(2\pi f t) \tag{2.14}$$

It is well known in sampling theory that the maximum resolvable frequency component without aliasing is given by

$$f_{max} = \frac{Fs}{2} = \frac{1}{2dt}, \tag{2.15}$$

where F_s is the sampling rate and dt the sampling time interval. Equivalently, we can write the maximum Δz, or ranging depth, as

$$z_{max} = \frac{\pi}{2\delta k} = \frac{\lambda_0^2}{4\delta\lambda}. \tag{2.16}$$

It can be seen that the ranging depth in OFDR is inversely related to the instantaneous line width of the swept laser. Similarly, it can be shown that an uncertainty relationship exists between δk and δz such that the axial resolution is given by [50]

$$\delta z = \frac{2 \ln 2}{\pi} \frac{\lambda_0^2}{\delta \lambda}. \tag{2.17}$$

This is the same axial resolution for the time-domain LCI approach and shows that the axial resolution is determined by the tuning bandwidth of the swept source.

In OFDR, the A-line rate is determined by the speed at which the wavelength swept source can be tuned. At the detector end, the signal should be digitized at a sampling rate such that the number of points per A-line, N, is greater than the instantaneous linewidth of the laser to avoid limitations in the ranging depth due to fringe washout [51].

$$N > \frac{\Delta \lambda}{\delta \lambda} \tag{2.18}$$

The depth reflectivity profile in OFDR is obtained by sampling, removing the DC terms, and performing a Fourier transform. As was shown above, each different value of Δz is encoded at a different frequency. Because the wavelength swept laser is linear in λ and not in k-space, the digitized data is first interpolated to evenly spaced k values prior to the Fourier transform.

2.4.2 Noise

The noise terms in OFDR are fundamentally the same as those present in LCI and include thermal, shot, and RIN noise terms. However, because the signal is encoded in frequency space, an SNR advantage can be achieved [36,44–46]. The total noise is still the sum of the individual noise terms multiplied by the detection bandwidth.

$$\sigma_n^2 = (\sigma_{th}^2 + \sigma_{shot}^2 + \sigma_{RIN}^2)BW \tag{2.19}$$

The detection bandwidth is equal to the sampling rate, Fs. Parseval's theorem allows us to relate the signal power in the time-domain and frequency-domain.

$$\sum |i[n]|^2 = \frac{1}{N} \sum |X[z]|^2 \tag{2.20}$$

Here, N is the number of data points used in the FFT and we've written the transform as a function of z because depth is directly encoded in frequency space. For a fixed reflector the right side of Eq. 2.20 is concentrated at single positive and negative frequency peaks and the total signal power can be written as

$$|F(z_0)|^2 = \frac{N_s^2}{2} < i_s^2 > \tag{2.21}$$

and the time-averaged noise power is still given by

$$< \sigma_n^2 >= N_s < i_n^2 > \tag{2.22}$$

Therefore, the SNR can be written as

$$SNR = \frac{< F_s^2 >}{< \sigma_n^2 >} = \frac{N_s}{2} SNR_{td} \tag{2.23}$$

and it can be seen that the FD-OCT design has an SNR advantage of $N_s/2$ over the time-domain approaches. For shot noise limited detection, the SNR can be written as

$$SNR_{OFDR} = (\frac{\eta}{h\nu})\frac{P_{sam}}{BW}\frac{N_s}{2}. \tag{2.24}$$

N_s can be written as $N_s = F_s/f_A$ and the bandwidth is given by $BW = 2 * F_s$ which leads to

$$SNR_{OFDR} = (\frac{\eta}{2h\nu})\frac{P_{sam}}{f_A}. \tag{2.25}$$

Therefore, the SNR in OFDR is determined by the sample power and the A-line rate.

2.5 Summary

Both LCI and OFDR are optical techniques that generate depth-resolved reflectivity profiles in biological samples. Depth in LCI is encoded by scanning the reference arm in an interferometer. The axial resolution is defined by the spectral bandwidth of the broadband laser source and the SNR is determined by the sample power and the detection bandwidth. Practical limitations limit the A-line rate of LCI systems and make them impractical for hand-held POC use due to the presence of motion artifacts. In addition, increasing the A-line rate reduces the system SNR below acceptable levels.

OFDR is the second generation technique of LCI and uses a fixed reference arm and a wavelength-swept laser, and depth is encoded in frequency space within the detected signal. The axial resolution is determined by the tuning range of the source and the ranging depth is determined by the instantaneous linewidth of the source. OFDR exhibits an SNR advantage over LCI such that higher A-line rates can be achieved at comparable SNR values.

THIS PAGE INTENTIONALLY LEFT BLANK

Chapter 3

Automated Algorithm for Human Breast Tissue Differentiation

3.1 Introduction

Chapter 2 discussed the developement of a portable, low-cost device based on low coherence interferometry (LCI) developed for FNA needle guidance [37]. Other groups have investigated the use of needle based optical probes for biopsy guidance based on imaging [30], or by direct measure of tissue optical properties such as multispectral reflection analysis [31], scattering coefficient [32], and refractive index [33] measurements.

The initial feasibility study performed on excised breast surgical specimens indicated that LCI may have the potential for classifying adipose and fibroglandular breast tissue based on the slope and standard deviation of the axial depth profiles [37]. The sample size for this study was small and the accuracy of LCI for breast tissue type diagnosis was therefore not evaluated. Furthermore, this data was analyzed in a semi-automatic fashion that is not suitable for clinical use; the minimum and maximum boundaries over which the data was analyzed were selected manually. Automatic, robust tissue classification is essential for a useful POC FNAB guidance device because it allows the physician to guide needle placement in real-time without the need for off line processing.

In this chapter, we present an automated algorithm for classifying adipose and fibroglandular breast tissues that includes an additional, independent parameter that quantifies LCI signal spatial frequencies. The accuracy of this algorithm was determined prospectively in a blinded fashion on a cohort of 260 biopsy correlated LCI scans from 58 patients. Intra-sample variability of the algorithm was also tested. Similar classification parameters were recently introduced to develop methods for computationally driven differentiation of human breast tissue [13]. However, to our knowledge, our study represents the first complete study to test the efficacy of such parameters for classification of human breast tissue.

3.2 *In-vitro* Study

The LCI system and probe were described in detail in chapter 2. Briefly, the LCI system consisted of a non-reciprocal fiber optic Michelson interferometer. A broadband SLD centered at 1310 nm with a FWHM bandwidth of 50 nm (Optiphase, Inc.) was used as a light source. The axial resolution was 15 μm in air, or 11 μm in tissue (n=1.4). Light from the source was transmitted through the first output port of a circulator and an 80/20 splitter, which directed approximately 750 μW to the sample arm. LCI depth scans (A-lines) were obtained at a rate of 40 Hz and the path length in the reference arm was scanned by illuminating a retroreflector mounted on a galvanometer-driven lever arm (Cambridge Technology, Model 6220). Light from the sample and reference arms were recombined and directed towards a polarization beam splitter and two photodetectors, enabling polarization diverse detection. Near shot noise limited detection was achieved with a maximum SNR of

101 dB.

The optical probe consisted of a single mode optical fiber inserted through the bore of a 23 gauge (~570 µm OD) FNA needle. No focusing lens was used. The needle was attached to a regular syringe through a hub (INRAD, Model 54501). The syringe was held within an FNAB gun. The fiber probe was designed to be simple and therefore inexpensive. Since the fiber core aperture was always at the needle tip, there was no uncertainty regarding the probe location and the interrogated tissue was directly in front of the needle location. Although the fiber probe was housed within an FNA needle, no tissue aspirates were collected during the measurements.

3.2.1 Experimental Design

Excised surgical specimens were collected, stored in 10% phosphate buffered saline (PBS) and data was collected at 37° C within 24 hours of procuring the samples. The needle and FNAB gun were secured onto a vertical translation stage as shown in Fig. 3-1. During imaging, samples were placed flat on a piece of corrugated cardboard within a Petri dish and positioned under the needle probe. The needle was lowered onto the sample until the fiber surface came into contact with the sample. Ten consecutive A-lines were collected at each site. Following imaging, the needle was raised, and the needle location was marked with India ink. The samples were then fixed in formalin. Histologic sections were obtained and stained with hematoxylin and eosin (H&E).

Histology slides were read by a pathologist who was blinded to the LCI data. Slides were randomly ordered in order to avoid bias from reading samples from the same patient consecutively. Histology samples were grouped into two critical cases for this application, adipose and fibroglandular tissue types. Fibroglandular tissues included benign fibrous

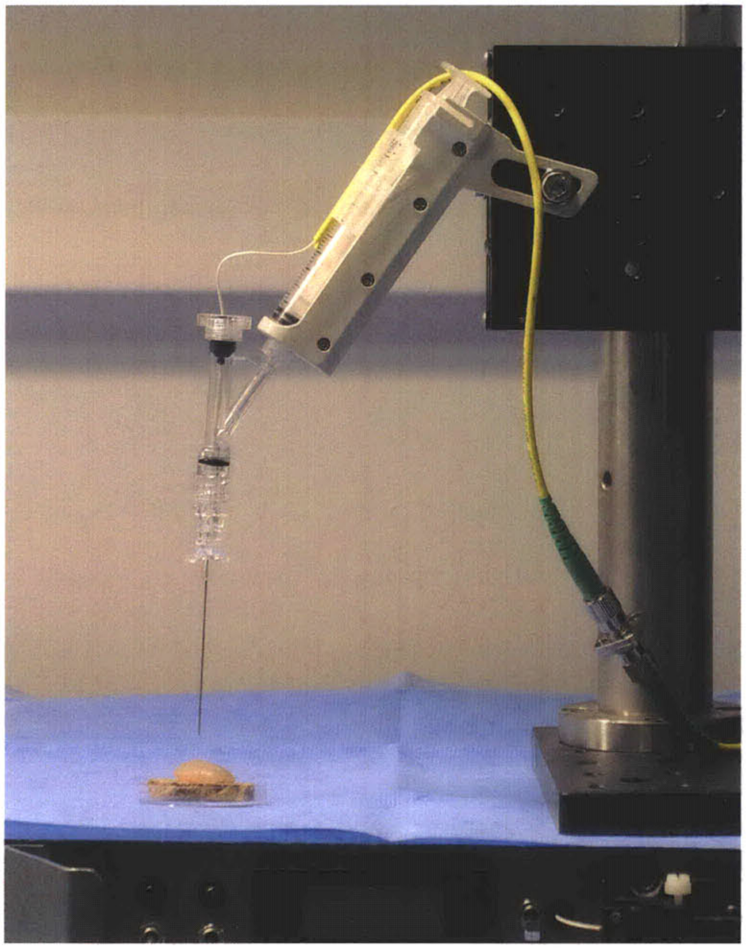

Figure 3-1: FNA gun mounted with needle and positioned above sample.

parenchyma, adenocarcinoma, and ductal carcinoma in situ (DCIS) tissue types. Only homogeneous samples classified as pure adipose, fibroglandular, or tumor tissue were included for parameter extraction and algorithm development/classification. Samples with significant heterogeneity in the image field as defined by the pathologist or samples where no ink was visible on histology were excluded. Heterogeneous samples were defined as tissues where the ratio of major to the minor tissue type was approximately less than 3:1 within one mm of the ink mark.

3.2.2 Parameter Extraction

For each sample, 10 consecutive A-lines were acquired. Signal parameters were extracted for each A-line and the mean value for each parameter was used to represent the sample. Each parameter was calculated using an automated MATLAB script without the need for additional user input other than the sample file. Prior to parameter extraction, the raw LCI interferogram data was converted to depth-dependent reflectivity profiles in the standard fashion [37]. The signal was transformed using DFT, band-pass filtered, frequency shifted to zero, and inverse transformed. The resulting linear intensity values were then converted to dB scale by $20\log_{10}$ multiplication.

Automatic LCI Scan Boundary Extraction

At the beginning and ends of the LCI scan, the signal contains data that is not representative of the tissue sample. As a result, prior to parameter extraction, the data must be automatically parsed to determine the segment of the LCI scan that contains tissue reflectivity information. The location of the fiber/sample interface was automatically determined by the following procedure. The noise floor was obtained by averaging the signal within the first 200 µm of imaging depth, which corresponded to a region proximal to the fiber/sample interface. All signal points below the threshold were set to be equal to the noise floor, using a threshold of 20 dB. Next, a first-order derivative was computed and the first peak was determined by the first zero crossing of the derivative. In order to avoid error from specular reflection at the fiber/sample interface, the start index was shifted an additional 100 µm beyond the first peak. Automatic selection of the beginning location of the LCI scan in this manner allowed the effective start index to always fall within signal values representing the tissue structure. The last 100 µm of the LCI signal was also skipped because the signal was generally low in this region. Thus, the analyzed data consisted of the region from the effective start index to the end of the LCI scan minus the last 100 µm. This algorithm was automated and applied to all LCI scans to determine the data range over which to compute the slope, standard deviation, and spatial frequency content parameters. The average depth over which the signal was analyzed was 936 µm with a range from 820 µm to 1.03 mm.

Slope

To first order, the LCI reflectivity intensity decreases in accordance with the Beer-Lambert law. At a source wavelength of 1300 nm, tissue optical properties are such that scattering dominates over absorption [52]. Therefore, the slope of the logarithmic axial depth profile is related to the scattering coefficient and can be used as a parameter for classifying tissue type. A higher slope indicates more attenuation and a larger scattering coefficient whereas a lower slope indicates a lower scattering coefficient. The slope was calculated by a first-order polynomial fit over the region of interest.

Standard Deviation

The variation of scattering cross-sections within an LCI depth scan can be used as another parameter for classifying tissue type. One way to assess the scattering variance is to measure the slope-subtracted standard deviation of the axial depth profile. If the scattering fluctuates significantly, the reflection profile will have peaks interspersed with periods of low signal and the standard deviation will be high. Conversely, if the scattering is relatively homogeneous, the signal will be more continuous and the standard deviation will be low. In order to remove the effect of the bulk averaged scattering coefficient, the residual of the linear fit was used to compute the standard deviation.

Spatial Frequency Content

Scattering center distribution, representing distance between scatterers, may be evaluated by analyzing the spatial frequency components of the signal. The power spectrum of the signal can be interpreted as the signal energy within spatial frequency windows and the unique signature from different tissue types was recently described as a method for differentiating human breast tissue [13]. The spatial frequency parameter was computed in the following manner. First, as with the computation of the standard deviation, the linear regression was conducted and the residual was utilized for subsequent processing. Next, the DC component was removed by mean subtraction. Data outside the start and end index were set to zero. The resulting signal was zero mean, with components that fluctuated with varying frequency content depending on tissue type. The DFT was then computed. The spatial frequency parameter was then defined by integrating the magnitude of the spatial frequency content over a particular window band. The window was defined by calculating the average DFTs for the entire training set and observing where the adipose and fibroglandular tissue samples differed. A zoomed portion of the mean DFTs for the training set are shown in Fig. 3-2. The vertical lines represent the width of the integration window.

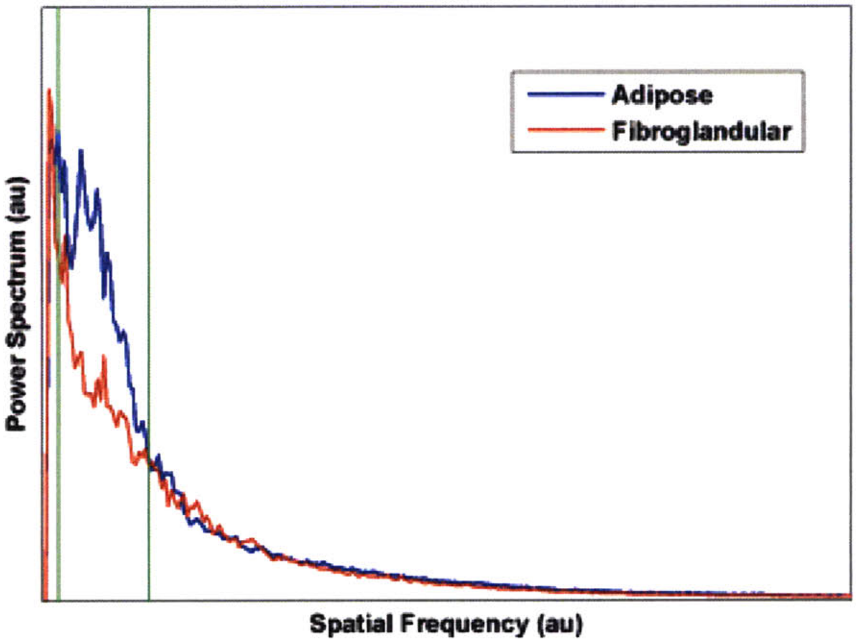

Figure 3-2: Average power spectrum data from LCI depth scans over the entire training set that show a region of difference between adipose and fibroglandular tissues types. The integration window (green lines) represents the area over which the spatial frequency content parameter is generated.

3.2.3 Algorithm Model

A multivariate Gaussian model was used for classification. The data set was randomly split into a training and validation set. A pooled estimate of the covariance matrix was used for the training set. The result of the model was an equation for each class that defined the probability that any new set of parameters fell within that class. Prospective analysis was then performed on the validation set. Classification was carried out by extracting parameters for each test sample, calculating the probability of falling within a particular class, and then assigning classification based on the highest probability.

3.2.4 Intra-sample Variability

In order to test the intra-sample variability of the device and algorithm an additional experiment was conducted using a separate data set. The needle probe was lowered onto each sample and a 10 A-line acquisition was performed. The needle was then raised off of the sample using the vertical translation stage and re-lowered back onto the sample for an additional 10 A-line acquisition. This process was repeated ten times so that each sample had 10 data sets of 10 A-lines each all from the same exact location. After the tenth measurement, the needle was raised and the sample was marked with India ink and sent for histology sectioning and staining. Each set of 10-alines was processed in the same manner as the early experiments so that a single set of extracted parameters characterized each set of A-lines. The samples were then classified using the multivariate Gaussian model. The result was a set of ten classifications, from the same sample, at the same location. The intra-sample variability was defined as the percentage of misclassified measurements within a particular sample.

3.2.5 Statistical Analysis

The accuracy of LCI for classifying breast tissue type was assessed by comparing the predicted tissue type to the "gold standard" histopathologic classification. All data processing and parameter extraction were done within MATLAB. Each parameter is listed as $\mu \pm \sigma$ where μ is the mean, and σ the standard deviation. The p-values were calculated using a two-sided unpaired t-test to determine if the difference in sample means between parameters were statistically significant. 95% Confidence intervals (CI) are also reported.

3.2.6 Results

Typical LCI profiles of adipose and fibroglandular breast tissue were very different (Fig. 3-3). The adipose samples contained multiple reflectivity peaks, presumably representing the lipid core and cell membrane interface. Human adipocytes range in size from 50-150 µm which makes the location of the reflectivity peaks highly variable [53]. The scattering centers in the fibroglandular tissue case are much closer together and most likely come from small changes in the refractive index from within the extracellular matrix. As a result, the LCI signal for fibroglandular tissue was smoother and more continuous.

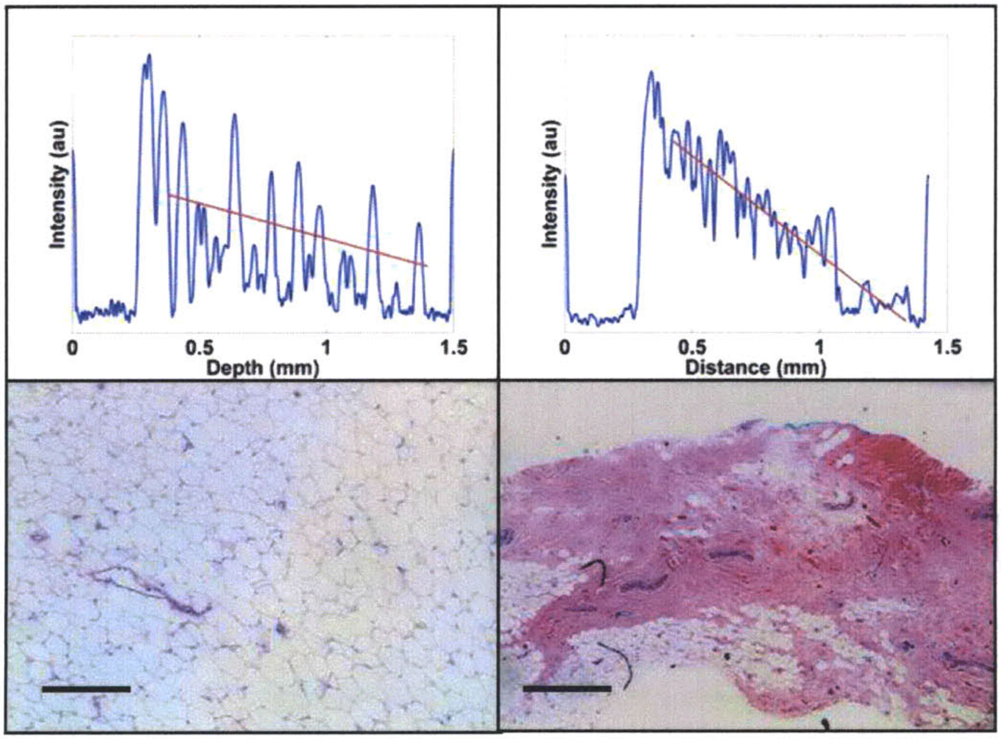

Figure 3-3: Characteristic axial depth scans from adipose (left) and fibroglandular (right) human breast tissue with corresponding histology sections. The red line is a first-order polynomial fit through the data. Intensity data shown in logarithmic scale. Scale bar equals 500 µm

Data was collected from a total of 260 samples from 58 patients. Of those, 34 were not analyzed due to the absence of a fiducial ink mark in the histopathologic slide and

54 were excluded owing to the presence of heterogeneous tissue (defined above) at the LCI measurement site. The set of 158 histopathology correlated LCI datasets included 71 adipose and 87 fibroglandular cases. The fibroglandular dataset included 71 benign fibrous parenchyma, 13 adenocarcinoma, and 3 DCIS cases. The datasets were randomly separated into a training set (n=72; 37 adipose, 35 fibroglandular) and a validation set (n=86; 34 adipose, 52 fibroglandular). There were 7 (5 Adenocarinoma, 2 DCIS) and 9 (8 Adenocarcinoma, 1 DCIS) tumor cases included in the fibroglandular group for the training and validation sets respectively. The additional samples were used for intravariability testing (N=14).

3.2.7 Training Set

The results from the training set are listed in Table 3.1. As the table demonstrates, each parameter has a significant p-value. The average magnitude of the slope parameter was higher for fibroglandular tissue, which indicates a higher scattering coefficient for fibroglandular breast tissue compared with adipose tissue. The mean standard deviation was higher for adipose tissue as a result of the signal variation resulting from refractive index fluctuations. The spatial frequency parameter had more energy for the adipose samples within the integrated window band. There was no spatial frequency region where the fibroglandular tissue had higher energy as was seen at higher spatial frequencies in Zysk et. al [13]. This could be due to differences in axial resolution (10 µm vs. 2 µm) since the Fourier Transform resolution is highly dependent on spatial sampling frequency.

Another way to represent the training data is through the use of a scatter matrix as shown in Fig. 3-4. The scatter matrix plots two dimensional scatter plots between each set of parameters and can be used to observe correlations between classification parameters. It

Table 3.1: Training set statistics

Parameter	Adipose (N=37)	Fibroglandular (N=35)	p
Slope	-1.74±.1.36	-4.39±2.23	$< 1.7x10^{-7}$
Std. Dev.	7.23±.1.54	5.41±0.71	$< 2.2x10^{-7}$
Spat.Freq.	1.42±.0.54	0.97±0.27	$< 2.2x10^{-9}$

can be seen that there is little correlation between the slope and standard deviation as well as the slope and spatial frequency parameters. In addition, the slope/standard deviation and slope/spatial frequency scatter plots show that the adipose and fibroglandular data sets fall into separate regions, making classification based on these parameters possible. The scatter plot matrix also shows that the standard deviation and spatial frequency parameters are highly correlated. This is expected as both parameters are related to the scattering strength and scatterer distribution. The correlation is higher for the adipose ($R = 0.938$) than for the fibroglandular ($R=0.780$) tissue samples.

3.2.8 Validation Set

The results from the validation set using all three parameters for classification are listed in Table 3.2. The classification parameters show the same trends as were seen in the training set data. The classification results using all three parameters for classification are listed in Table 3.3. Since during an FNA procedure the collection of adipose tissue is seen as a non-diagnostic result, the correct classification of adipose tissue can be viewed as a true negative, and the correct classification of fibroglandular tissue can be viewed as a true positive. In this way, the sensitivity, as defined by TP/(TP+FN) is equivalent to the accuracy of detecting fibroglandular tissue. In addition, the specificity, as defined by TN/(TN+FP) is equivalent to the accuracy of detecting adipose tissue. The sensitivity and specificity of the validation set were 98.1% (95% CI: 89.7-99.9) and 82.4% (95% CI: 65.5-93.2) respectively. The overall

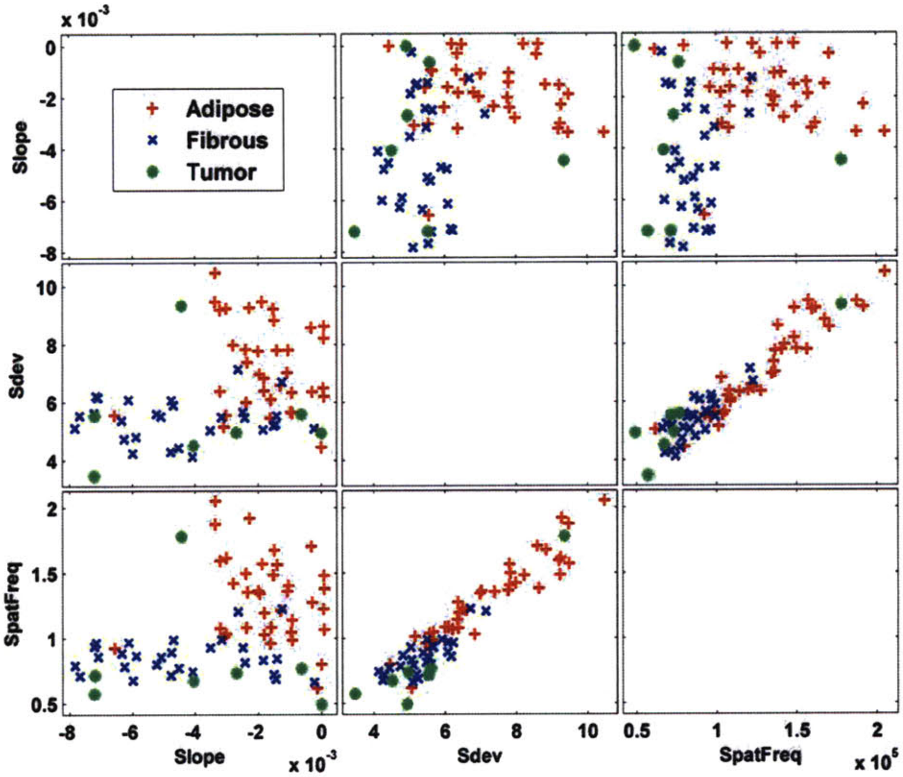

Figure 3-4: Scatter plot representation of the entire training set data that can be used to visualize relationships between parameters. There is a high degree of correlation between the standard deviation and the spatial frequency content parameters for both the adipose (red plus sign) and fibroglandular (blue cross) tissue types. Tumor tissues labeled in green circles were included in the fibroglandular tissue classification.

accuracy was defined as the total number of correctly classified tissue samples regardless of tissue type. With 86 (34 adipose, 52 fibroglandular) samples in the validation set the overall accuracy was 91.9% (95% CI: 84.0-96.7). Confidence intervals were calculated by using the normal approximation to the binomial distribution [54]. The one misclassified sample from the fibroglandular validation set was an adenocaricnoma case. The other 8 of 9 tumor cases were correctly classified as fibroglandular tissues.

Table 3.2: Validation set statistics

Parameter	Adipose (N=34)	Fibroglandular (N=52)	p
Slope	-1.69±.1.25	-5.04±2.21	$< 1.9x10^{-11}$
Std. Dev.	6.92±.1.35	5.51±1.55	$< 7.0x10^{-5}$
Spat.Freq.	1.23±.0.31	0.82±0.23	$< 4.6x10^{-9}$

The above results use all three classification parameters as described above. In order to determine whether or not the three parameter model was statistically better than simply using the slope and standard deviation parameters [37], it was necessary to look at a truth table describing the differences between the two models. The overall classification results using only the slope and standard deviation parameters are shown in Table 3.4. The sensitivity and specificity were 80.8% (67.5-90.4) and 82.4% (65.5-93.2) respectively. Using only the two parameter model 4 tumor cases, all Adenocarcinoma, were misclassified as adipose tissue. A truth table to quantify the differences between the two models is shown in Table 3.5. In Table 3.5 a +/+ cell indicates that both the 2-parameter and the 3-parameter models correctly classified the sample. A +/- cell indicates that the 2-parameter model correctly classified a sample whereas the 3-parameter model misclassified a sample. Similarly, a -/+ cell indicates that the 3-parameter model classified the sample correctly when the 2-parameter model misclassified the sample and the -/- cell are samples that both models misclassified. The table shows that there are nine cases where the 3-parameter model classified a fibroglandular sample correctly when the 2-parameter model misclassified the sample, and no cases with the reverse scenario. The associated p-value is calculated using the McNemar's test for correlated proportions and shows that there is a statistically significant difference between the two and three parameter models in terms of fibroglandular tissue classification. No statistical difference was observed for the adipose case.

Table 3.3: Classification results for 3-parameter model.

		Predicted Class	
		Adipose	Fibroglandular
True Class	Adipose	29	5
	Fibroglandular	1	51

Table 3.4: Classification results for 2-parameter model.

		Predicted Class	
		Adipose	Fibroglandular
True Class	Adipose	28	6
	Fibroglandular	10	42

Table 3.5: Model comparison.

		3-parameter Model			
		Fibroglandular		Adipose	
2-parameter Model		+	-	+	-
	+	42	0	26	3
	-	9	1	2	3
		$p < 0.01$		$p < 1$	

Since the standard deviation parameter is calculated from the slope-subtracted LCI signal, errors in the slope calculation could result in an artificially high standard deviation measurement. In order to test the effect this would have on our classification, we simulated errors in the slope by randomly modifying the slope parameter to +/- 5,10, and 20% of its nominal value. The standard deviation and spatial frequency content parameters were then recalculated using the modified slope value. The resulting classification was compared to the nominal value result using the McNemar's test as described above. There was no significant difference in the classification results for either the adipose or fibroglandular tissue type. For the maximum error of +/- 20%, the sensitivity was 96.2% (95% CI: 86.8-99.5) and the specificity was 76.5% (95% CI: 58.8 - 89.3).

3.2.9 Intra-sample Variability

Data to test intra-sample variability was collected and analyzed from a separate set of 14 samples from 6 patients (6 adipose, 8 fibroglandular). The average intra-sample variability was 18.3% (95% CI:9.5-30.4) for adipose and 1.3% (95% CI:0.03-6.8) for the fibroglandular tissue samples. The overall Cohen's kappa statistic was 0.821 (95% CI:0.725-0.981). The number of errors for each 10 A-line set was as follows: Adipose [1 0 0 0 7 3] and Fibroglandular [0 0 0 1 0 0 0 0]. The one outlier sample within the adipose data set (7/10 error rate) was due to low signal content which tended to reduce the Spatial Frequency Content parameter and shift the probability towards the fibroglandular tissue type. If the outlier would be removed, the adipose intra-sample variability rate would become 8.0% (95% CI:2.2-19.2) and the kappa value would become 0.918 (95% CI:0.847-0.988).

3.3 Discussion

We have developed an automated algorithm for differentiating ex vivo adipose tissue and fibroglandular human breast tissue using low coherence interferometry that achieves a high sensitivity and specificity. The extracted parameters used for classification are simple and require minimal additional computation time compared with the standard post-processing of the LCI signals. The goal of this project is to differentiate between non-diagnostic adipose tissue and the fibroglandular tissue more likely to harbor disease. The ability of LCI to differentiate between adipose and fibroglandular tissue indicates that this technology has the potential for being a useful tool in FNA procedures in an attempt to reduce non-diagnostic sampling rates. More importantly, tumor samples are correctly classified as fibroglanduar meaning that they won't be misclassified as adipose tissue, resulting in a missed diagnosis.

There remain a few challenges to taking such a system into an FNA clinic. First, in this work only homogeneous samples were used for analysis and classification. This was done in order to define a clear set of parameters that represent the true nature of adipose and fibroglandular tissue types. In a clinical setting, heterogeneous samples will be encountered which will decrease the accuracy of the model. Future work will focus on further defining boundaries between tissue types to provide a regional diagnosis that will account for heterogeneity. In addition, some clinical applications may require further differentiation of fibroglandular tissues into normal fibrous and tumor tissue types as well as identification of additional categories such as necrotic tissue. The classification of non-diagnostic adipose tissue samples, however, does not require this distinction, and as such, was outside the scope of this study. Also, LCI assumes that the signal comes from single scattering events, but the presence of multiple-scattering, especially at larger depths within the sample can lead to decreased resolution, and changes in the signal profile. In particular, the slope parameter, with its connection to the Beer-Lambert law is particularly sensitive to the single-scattering assumption. It may be necessary to define the border between single and multiple-scattering in order to improve the model and include additional tissue types. In addition, since the standard deviation parameter is calculated from the slope-subtracted LCI scan, any error in the slope fit could result in artificially high standard deviation measurements. However, we found that errors up to +/- 20% did not significantly affect the classification result.

Insertion of the LCI needle probe within the tissue structure in an *in vivo* setting, as opposed to surface only measurements as when done in this study, may introduce additional obstacles that could limit the algorithm's effectiveness. Issues such as bleeding, tissue or optical fiber compression, and operator motion artifacts will all come into play. We plan on studying these issues through in vivo animal experiments to further define any limitations of the LCI needle probe. We anticipate that higher speed systems will significantly reduce any motion artifacts seen in the current device. Lastly, the ability to collect collect tissue aspirates directly following an LCI measurement will need to be addressed. Issues such as the collection of sufficient aspirate material as well as the development of a disposable probe are the subject of ongoing investigation.

Another important area of research, and the focus of the rest of this thesis, is system speed improvement, miniaturization and simplification. The LCI system used in this study was about the size of a briefcase and not suitable for hand-held clinical use, a necessity for POC FNAB guidance. In addition, imaging at only 40 A-lines/sec leaves the system susceptible to motion artifacts. Chapters 4 and 5 discuss enabling technologies for making a truly hand-held optical needle guidance system. Chapter 4 presents a novel novel miniature wavelength-swept laser suitable for POC OFDR. OFDR is the second generation improvement of LCI as discussed in chapter 2 and allows us to take advantage of improved SNR, higher speed imaging, and greater imaging depth [36]. This laser is about the size of a deck of cards, can be fully battery powered, and is capable of peak optical power and tuning speeds approaching current swept sources used in clinical OFDI systems. Chapter 5 then discusses the use of reduced bit-depth acquisition to reduce the data storage demands while maintaining imaging speed in OFDR and OFDI. This is important for building a small, simple, and portable POC device for FNAB.

Chapter 4

Miniature Swept Source

4.1 Introduction

As was discussed in chapter 3, one example where optical point-of-care (POC) technologies can make a difference is in the setting of Fine Needle Aspiration biopsy (FNAB). One challenge for the system and algorithm presented in chapter 3 is imaging speed. The LCI system only generated 40 A-lines/sec, which is not suitable for hand-held clinical use. In addition, the entire system was about the size of a briefcase. In this chapter we present a novel miniature swept laser suitable for optical frequency domain imaging (OFDI) for use in POC optical technologies such as FNAB guidance.

The development of high-speed wavelength-swept lasers for OFDI has advanced at a rapid pace. There are several commonly applied designs for these sources. One common design uses a semiconductor gain medium within a unidirectional fiber ring cavity and an intracavity or extended cavity swept wavelength filter. Swept wavelength filters can be comprised of a diffraction grating and polygon mirror [47], galvanometer scanning mirror [55], or scanning Fabry-Perot filters [48, 49]. Other designs allow all wavelengths to propagate within the cavity and control the round-trip such that a single wavelength returns to the tuning filter at harmonics of the round trip time. These designs are known as Fourier Domain Modelocked Lasers (FDML) and can achieve very high sweep rates in excess of 300 kHz [56]. Linear cavity laser designs have also been employed where wavelength-tuning is achieved by diffraction grating/reflecting mirror combinations [57–60]. Linear cavities often provide a bidirectional wavelength sweep where differences in forward and backward sweep dynamics are determined by cavity length and tuning speed [61]. Common to all designs, however, is a prohibitively large form-factor for POC deployment.

In this chapter we present a high-speed, high-power, miniature wavelength swept laser for use in POC OFDI applications. The laser utilizes a linear cavity design and can achieve 12 mW of peak output power, a 75 nm tuning bandwidth, and 0.24 nm instantaneous line width. The laser has a bidirectional sweep rate of 15.3 kHz enabling 30.6 kHz OFDI A-line generation. In addition, the entire laser can be operated on battery power and packaged in a form factor that's roughly the size of a deck of cards.

4.2 Experimental Setup

4.2.1 Laser Design

Figure 4-1 shows the source design based on a tunable optical filter using a reflection grating and a miniature resonant scanning mirror. The gain element of the laser was a single angle facet (SAF) gain module (Covega, Inc. SAF 1136), in which the waveguide was terminated at one end by a normal-incidence facet at 90% reflection, forming an output coupler, and at the second end by an angled facet at 0.01% reflection, which delivered light to an external cavity [62]. Wavelength selection was accomplished using a 1200 l/mm diffraction grating, oriented to an angle of incidence of approximately 80 degrees, followed by a resonant scanning galvanometer mirror (Electro-Optical Products Corp. SC-30) and a fixed mirror. The external cavity was approximately 8 cm.

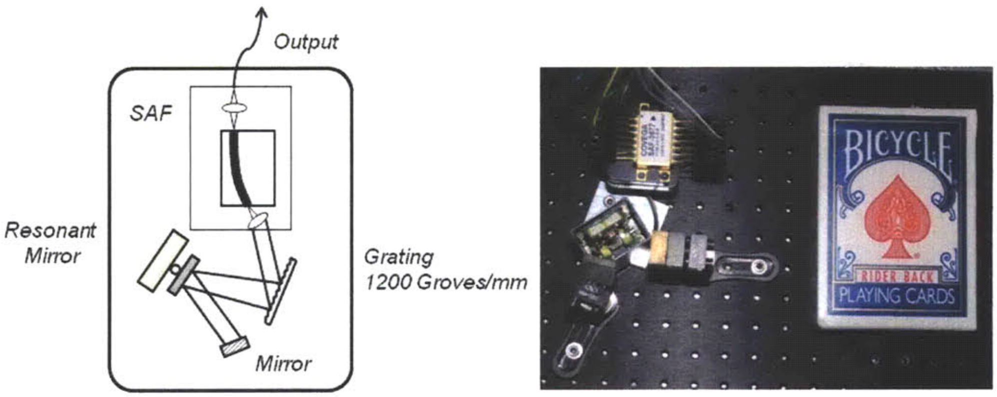

Figure 4-1: Miniature wavelength-swept laser source schematic (left). The output from a semiconductor gain medium illuminated a grating and was deflected via a resonant scanning mirror such that only one wavelength of light was amplified within the laser cavity. As the resonant mirror rotated, the lasers output wavelength was swept in time. A photograph of the source (right) is shown adjacent to a pack of cards for scale.

Light from the gain medium was dispersed by the grating according to the familiar grating equation $\lambda = p(\sin\alpha + \sin\beta)$, where λ is the incident wavelength, p the grating pitch, and α and β the incident and diffracted angles respectively. The FWHM bandwidth of the filter is determined by the grating pitch, incident angle, and beam diameter and given by $(\delta\lambda)_{FWHM}/\lambda_0 = (4\ln 2)^{1/2}/\pi * (p/m)\cos\alpha/W$, where m is the diffraction order, and W is the $1/e^2$ width of the Gaussian beam [47]. The beam width was approximately 0.5 mm corresponding to a $(\delta\lambda)_{FWHM}$ of 0.21 nm.

The tuning bandwidth of the filter is given by $\Delta\lambda = p\cos(\beta_0)\Delta\beta$, where $\Delta\beta$ is the physical scan angle of the resonant scanner and β_0 is the output angle at the center wavelength. It should be noted that resonant scanner scan angles are sometimes reported as optical scan angle which is equal to double the physical scan angle of the mirror. In this chapter, we refer to $\Delta\beta$ as the physical scan angle. Resonant scanners have scan angles that decrease with increasing frequency. At 15.3 kHz, the scan angle was only ~3 degrees. Therefore the resonant scanner was further deflected onto a fixed mirror to work in the so called "2X" configuration and double the filter's effective scan angle. Similar configurations have been used to increase the FSR by using multiple mirror reflections [62, 63]. At 6 degrees total optical deflection, the tuning bandwidth was 69.1 nm which makes the theoretical finesse 329.

Even though the gain bandwidth is broader than the filter free spectral range and the filter tuning range lies within the gain bandwidth, the duty cycle of the laser is further limited by the physical size of the resonant and fixed mirrors as well as their distance from the diffraction grating. In order to utilize the entire scan angle of the resonant scanner, the resonant scanner must be placed close enough to the diffraction grating to avoid clipping of the optical beam at the edge of the resonant scanning mirror. It can be shown that the distance restriction for the 2X configuration is given by $r < d/\tan\Delta\beta - 2W\cos\beta_0/\cos\alpha$. Here, d is the physical size of the resonant mirror (4 mm) and r is the distance from the grating to the resonant mirror. A similar expression can be derived for the distance between the resonant and fixed mirrors. If these restrictions are met, and the tuning bandwidth is entirely within the gain-bandwidth of the gain medium, the laser will have 100% duty cycle. Otherwise, if the scan angle is increased such that the tuning bandwidth is outside the gain bandwidth or the beam is clipped, the duty cycle will be less than 100%. Currently, the resonant mirror size cannot be increased without decreasing the resonant scan frequency.

The resonant mirror was driven with a high-Q resonant electric drive circuit (Electro-Optical Products Corp., ED-M) that required very low electrical power. It can be operated for long periods of time with a 9V battery. The laser source was driven with commercially available miniature laser (Wavelength Electronics FL500) and temperature (Wavelength Electronics WTC 3243 HB) controllers and powered by 3V lithium batteries. The entire laser, including optics and electronics was configured with a form factor that is approximately the size of a deck of cards (Fig. 4-1). The actual physical size of the laser optics was 3 in. x 2.5 in. x 3 in.

4.2.2 OFDI imaging setup

The OFDI imaging setup is shown in Fig. 4-2. The laser output was directed through an 80/20 splitter into sample and reference arms. Each arm consisted of a circulator and signal reflection elements. During calibration and testing, a fixed reflector was placed in both the reference and sample arms. During imaging, the sample arm consisted of an X-Y galvanometer scanner (Cambridge Technology 6220H), and a 30 mm focal length lens. The reference arm contained a neutral density attenuator to control the power on the detector. The signals were recombined through a 50/50 splitter and directed input into an 80 MHz balanced receiver (New Focus 1817). The signal was digitized at 50 MS/s with a 14-bit DAQ (Gage: CompuScope 14200). The A/D acquisition was triggered directly from the TTL output of the resonant scanner driver. Samples were re-interpolated to equal spacing in K-space [36].

4.3 Results

4.3.1 Laser characteristics

A characteristic laser output trace is shown in Fig. 4-3. The peak output power was ~12 mW (6.0 mW average power) with only subtle power differences between the forward and backward wavelength sweeps. The green trace is the TTL signal from the resonant

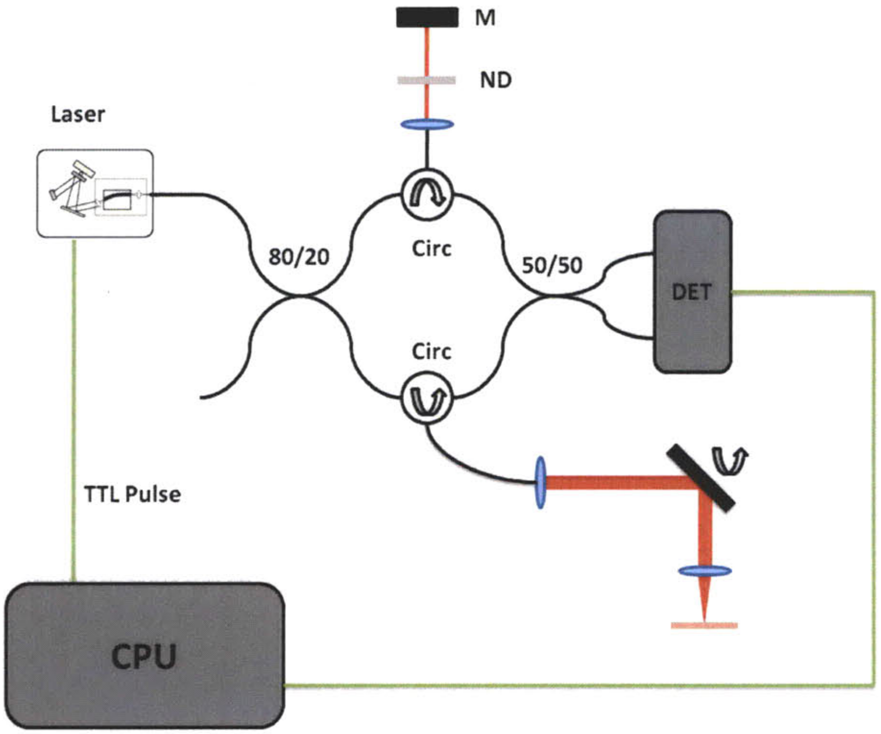

Figure 4-2: OFDI Imaging setup. The output from the swept laser is directed through an 80/20 splitter into reference and sample arms. Each arm contains a circulator and signal reflection elements. The reference arm consists of a neutral density filter and a fixed mirror (M). The sample arm contains a two-axis galvanometer scanning system. The dual balanced detector (DET) output into a computer (CPU) for digitization and processing. The resonant scanner TTL pulse is used for acquisition triggering.

driver. The resonant frequency was measured to be 15.3 kHz. The transition from forward to backward sweep direction occurred within the gain bandwidth of the SAF, resulting in continuous lasing during this transition. During this transition, the speed of the resonant scanner eventually slows to zero and a highly non-linear scanner motion occurs. The plateau and dip may be a mismatch between the linear sampling of the detection electronics and the non-linear motion of the resonant scanner. The cavity mode spacing was 1.9 GHz which may have contributed to the high-frequency noise seen in the laser trace. The overall duty cycle was 87.6%. The laser produced an edge to edge tuning range of 75 nm (Fig. 4-4) centered at 1340 nm. The spectrum was taken by applying the max-hold function on the optical spectrum analyzer (OSA) (HP 70950B) at 0.2 nm resolution to avoid mismatch between the laser sweep rate and the OSA sampling rate. The sharp peaks at short wavelengths in the scan are the sinusoidal scan pattern, resulting in increased time spent at the edges. The increased tuning range compared with the theoretical result is attributed to slightly larger scan angle of the resonant scanner.

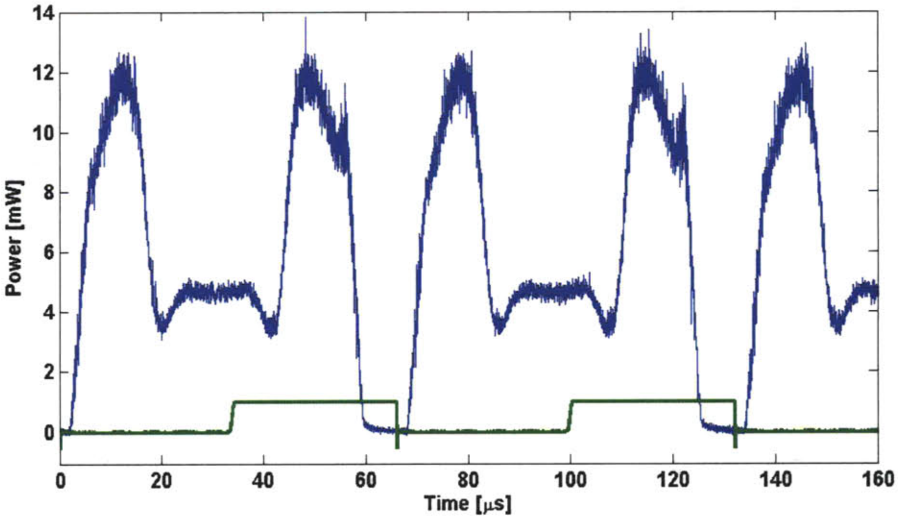

Figure 4-3: Laser trace showing ~2.5 full sweeps of the resonant scanner. Green trace is the TTL output from the resonant scanner and used as the system trigger.

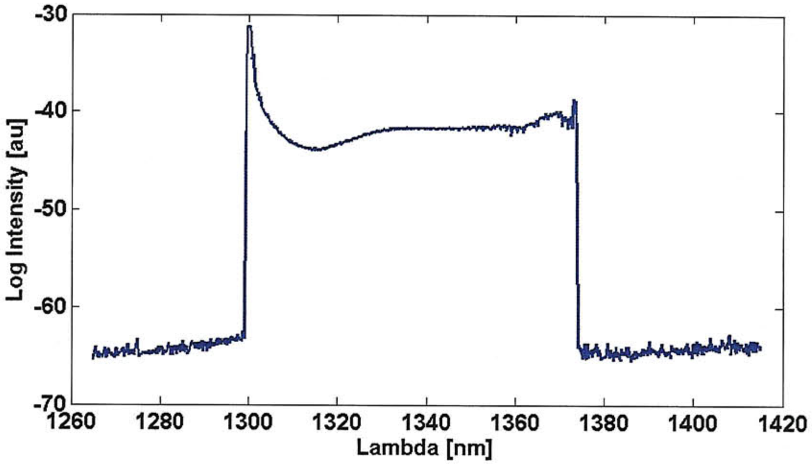

Figure 4-4: Tuning bandwidth, shown in log scale. The peaks at the edges are a sampling artifact as a result of the sinusoidal non-linear drive of the resonant scanner resulting in increased time spent at the edges.

After splitting the light into sample and reference arms and accounting for any interferometer losses, there was 4.2 mW of average power at the sample. A variable neutral density filter was adjusted such that 18 µW of power returned to each detector from the reference arms. The total sample arm power returning to the detectors from a fixed reflector was 2.5 mW. The fringe pattern from a fixed reflector is shown in Fig. 4-5.

The sensitivity and ranging depth were measured with a 43.5 dB attenuator in the sample arm path. The result from a fixed reflector at 500 µm for both forward and backward wavelength sweeps is shown in Fig. 4-6. The maximum sensitivity measured at zero delay was 98.1 dB. The dynamic range for the sensitivity measurement was 54.6 dB. The theoretical sensitivity including all noise sources was 100.3 dB with a shot noise limited sensitivity of 116.1 dB. The difference results from incomplete RIN noise suppression and thermal noise which were dominant over shot noise at the operating conditions. Figure 4-7 shows the SNR drop-off as a function of depth. The ranging depth as measured by the 6 dB drop in SNR was ~1.75 mm, indicative of an instantaneous linewidth of 0.24 nm, approximately 13% broader than predicted (0.21 nm). We attribute this to sub-optimal collimation from

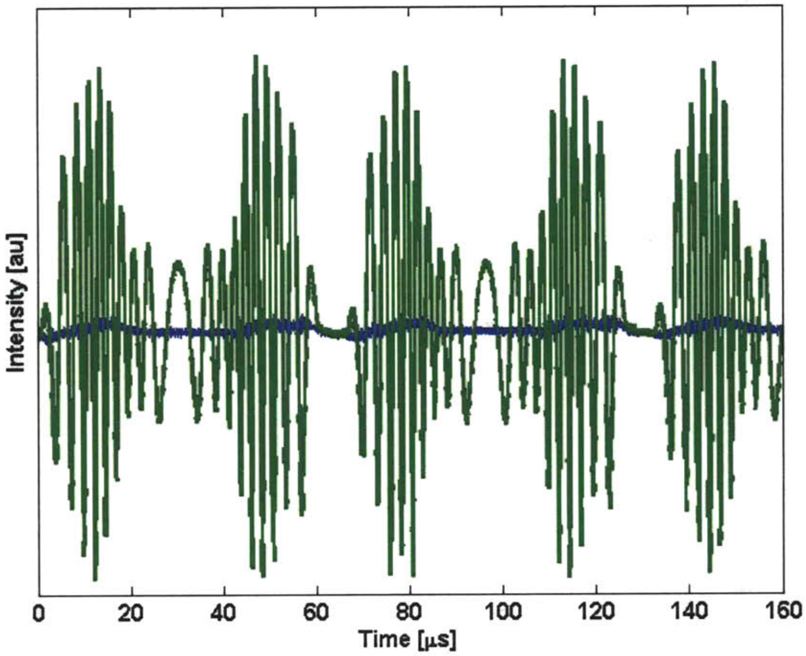

Figure 4-5: Characteristic fringe pattern (green) from a fixed reflector. Dual-balanced reference trace is shown in blue.

the SAF which decreases the effective beam size as well as errors from the interpolation into K-space which affect the 6 dB roll off calculation.

4.3.2 Battery powered operation

We have tested the battery-powered operation for over an hour with only minimal drop in output power (Fig. 4-8). This operating duration may be sufficient for point-of-care deployment in which a 10-15 minute operation is anticipated followed by recharging time between applications.

4.3.3 OFDI Imaging

Images obtained from the ventral surface of a human finger are shown in Fig. 4-9. The image is a 5 mm transverse sweep with 300 A-lines per frame, shown at 8-bit resolution. Images

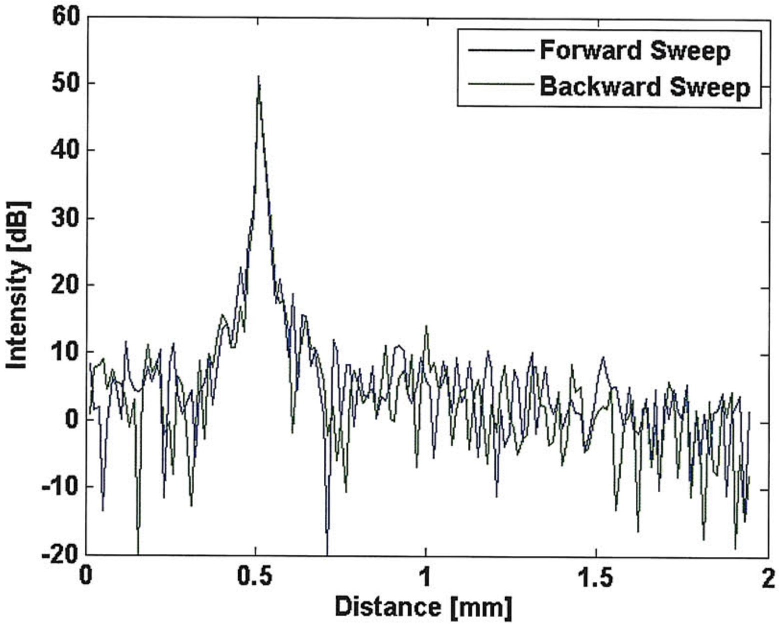

Figure 4-6: Axial point-spread function from a fixed reflector at 500 μm taken with a 43.5 dB attenuator in the sample arm. The forward sweep (blue) and backward sweep (green) are nearly identical in both SNR and axial resolution.

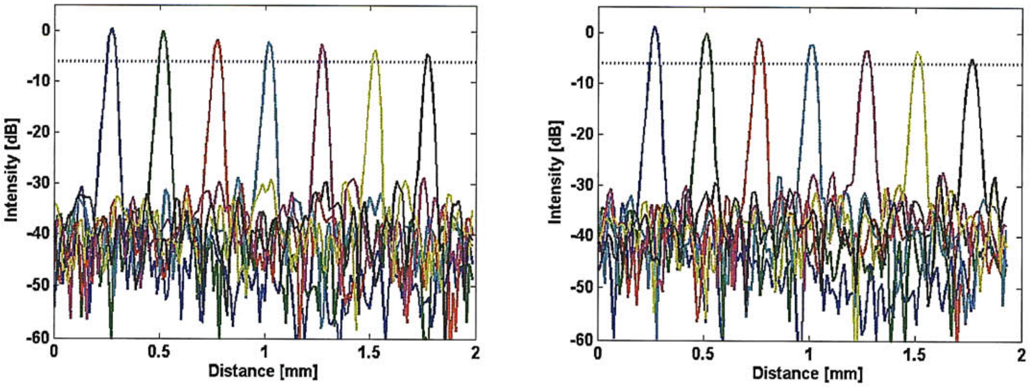

Figure 4-7: Signal roll-off as a function of depth for the forward (left) and backward (right) wavelength sweeps. Both sweeps can achieve > 1.75 nm ranging depth as measured by a 6 dB drop off in SNR from that at zero delay.

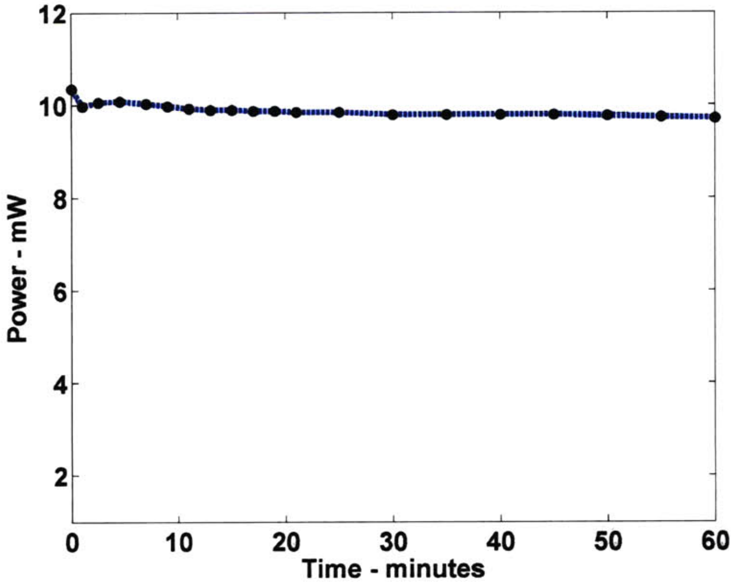

Figure 4-8: Laser output power as a function of time on full battery power. Minimal power loss is observed with over an hour of continuous use.

from the forward, backward, and combined (average of forward and backward) wavelength sweeps are presented. There were negligible differences between the forward and backward sweep images. The capability of our system to utilize both forward and backward sweeps enables imaging at the full 30.6 kHz rate provided by the source, which can also employed to reduce speckle noise as shown in the combined image.

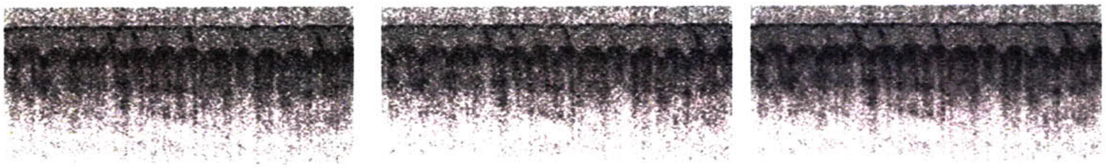

Figure 4-9: 5 mm x 2.25 mm OFDI images from the ventral surface of a human forefinger. Forward (left), backward (middle), and combined (right) wavelength sweep images.

4.3.4 Comparison of LCI and OFDR

We directly compared the LCI system used in chapter 3 and the new miniature swept source OFDR system described in this chapter by collecting depth-reflectivity profiles using the same probe for each system. The probe was the same angle cleaved single mode fiber described in chapter 3. Figure 4-10 shows representative depth-reflectivity profiles from both fibrous and adipose tissues. The general signal profile is expected to be the same because the central wavelength used in the two systems are nearly identical (1310 nm vs. 1340 nm) which makes the absorption and scattering properties similar. It can be seen that the OFDR system achieves greater imaging depth (1 mm vs. 1.5 mm) and greater signal dynamic range (35 dB vs. 40 dB).

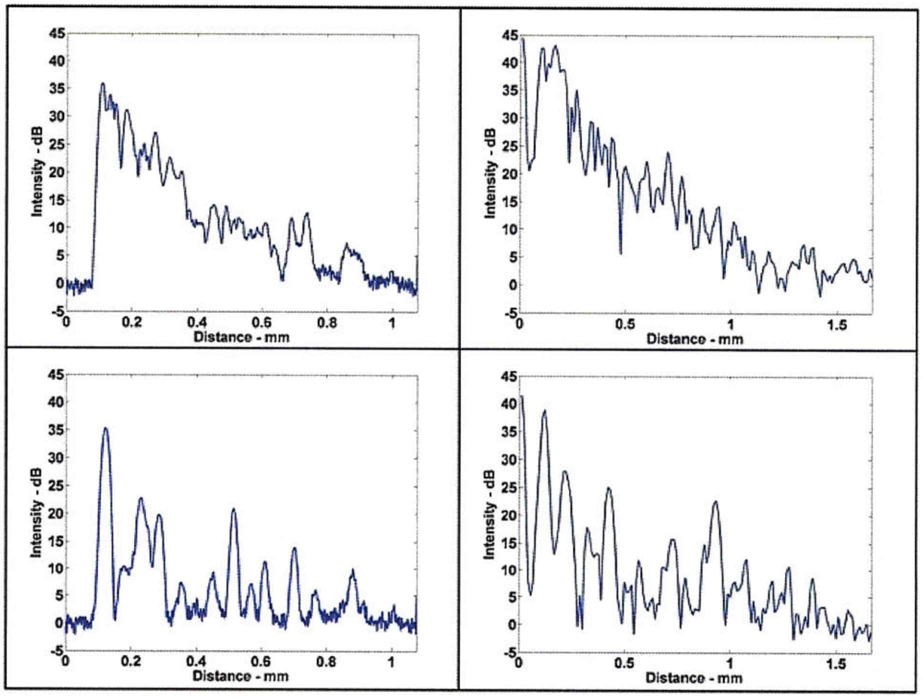

Figure 4-10: Comparison of LCI (left) and OFDR (right) depth reflectivity profiles from fibrous (top) and adipose(bottom) human breast tissue.

4.4 Discussion

A truly point-of-care OFDI system requires a small, portable, and fully packaged swept laser, interferometer, and detection, processing, and display electronics. We have focused only on the laser portion in this chapter and shown the capability of a miniature, battery-powered laser for producing high quality OFDI images. There remain a number of limitations and challenges towards implementing this design in a clinical POC system. First, although the laser optics are only the size of a deck of cards, the drive electronics require additional space. Together, the commercially available laser driver, temperature controller, and resonant scanner drivers would fit into a package roughly the size of 2-3 decks of cards including the batteries that drive each component. A fully custom built drive circuit could incorporate all the drivers onto a single printed circuit board to minimize the electronic footprint. Similarly, a custom battery cell and appropriate voltage regulators could be used to replace the three separate batteries we used in this study. Moreover, a fully packaged source may require additional temperature cooling to keep the laser output stable. The resonant scanner design also provides challenges for making the laser hand-held. Movement and vibrations can disrupt the resonant scanning mechanism. The resonant scanner used in this study has a counterweight that is used to achieve high scan speeds and improve stability. We have picked up the laser system and observed only small fluctuations in the SNR from a fixed reflector. The susceptibility of the laser output to motion and handling has not been tested in a systematic way and we expect that further work will be needed to design the packaging to ensure that the resonant scanner is highly stable.

The overall laser performance is determined by the filter efficiency and the drive current within the gain medium which sets the cavity gain. There is an inherent tradeoff between grating efficiency and filter linewidth. In order to achieve a sufficiently narrow linewidth required an incident angle of $\sim 80^\circ$ which is well away from the blaze angle of $\sim 36.5^\circ$. The efficiency-linewidth product can be improved by using a SAF with a larger beam diameter, allowing a shallower incident angle onto the grating for the same resolution. In addition, the gain medium current was limited to 500 mA which is the maximum current the miniature laser driver can achieve. A driver that can provide more drive current should improve the output power and improve the system sensitivity. However, increased drive current requires more battery power, which would reduce the operating time of the laser system. The small scan angle of the resonant scanner limits the tuning bandwidth. Larger scan angles can be achieved by reducing the resonant frequency.

The interferometer and detection electronics also need to be miniaturized for a POC OFDI system and the components used in this study are not suitable for fully portable use. One solution would be to use a common path interferometer that only requires a single circulator attached to the imaging probe. Common-path approaches have additional challenges such as setting the reference light appropriately to achieve good SNR and an inability to work in dual balanced mode. Similarly, the imaging optics used in this study are large and have high power consumption. In this study they were only used to demonstrate the imaging capabilities of the laser and a portable imaging system would require distal optics such as MEMS based scanners to generate an image.

A truly portable, battery powered source and OFDI system are not necessary for every POC application. Many clinical settings have access to power outlets and sufficient space to accommodate a cart based device. However, a fully portable OFDI system, including this laser design, would allow OFDI systems to be used in a broader range of clinical applications including ambulatory emergency medical services as well as battlefield medicine and in the austere settings of developing countries.

4.5 Summary

We have built a novel miniature wavelength-swept laser suitable for POC OFDI. The system can be fully battery powered, has a small footprint, and achieves a peak output power of 12 mW, 75 nm tuning bandwidth, and 0.24 nm instantaneous linewidth. Wavelength tuning is accomplished by using a reflection grating and a miniature resonant scanning mirror rotating at 15.3 kHz. Utilizing both forward and backward wavelength sweeps enables OFDI imaging at 30 kHz A-line rates. Images of the ventral surface of a human finger were obtained with good imaging depth and sensitivity. In addition, a direct comparison of LCI and OFDR depth-reflectivity profiles were obtained, showing that OFDR is equivalent or superior to the LCI system utilized in our prior studes.

THIS PAGE INTENTIONALLY LEFT BLANK

Chapter 5

Reduced Bit-Depth Data Acquisition

5.1 Introduction and Motivation

The most important feature of optical frequency domain imaging (OFDI) is its very fast image acquisition speed, which enables wide-field imaging studies *in vivo* [40–42]. Since the interferometric ranging signal in OFDI is collected in the Fourier domain, high-speeds can be achieved while maintaining sufficient detection sensitivity [44–46]. With the advent of rapid-scanning wavelength-swept lasers [47, 48, 63, 64], the speed of clinically-viable OFDI systems is currently limited by digital acquisition and storage capabilities. The relationship between imaging speed and the required digital throughput is determined by several factors, but the minimum necessary sampling rate is generally given by $f_A * N$ where f_A is the A-line rate and N is the number of points per A-line. N is given by $2 * \Delta\lambda/\delta\lambda$ and $\Delta\lambda$ and $\delta\lambda$ are the wavelength sweep range and instantaneous line-width of the laser, respectively. In addition, polarization diversity or polarization-sensitivity is highly desirable for robust clinical systems and doubles the required digital throughput.

In order to preserve the inherent dynamic range of OFDI, systems have typically utilized 12, 14 or 16 bit-depth digitizers. A typical polarization-diverse system, based on an 100 kHz repetition rate laser, capable of generating 195 images per second (512 A-lines per image), would therefore require a data throughput rate of 819.2 MB/s at 2048 points per A-line and assuming each sample is transferred as a two byte (16 bit) word. Clinical imaging with such a system may generate total data volumes in excess of 100 GB per patient and ten's of terabytes per study. Lowering the bit depth of acquisition would be a simple strategy for reducing data rates and volumes while also making it possible to utilize a broader range of fast digital acquisition electronics.

In the context of point of care (POC) optical frequency domain ranging (OFDR), data transfer and storage is not the only concern. One challenge is that currently available data acquisition (DAQ) systems of sufficient speed are too large and do not fit within our desired form factor. For instance, the 15.3 kHz system described in chapter 4 requires a sampling rate of roughly 50 MS/s to achieve good image quality. Even a slower speed system at 1kHz A-line rate would require 5MS/s. It is common in OFDI imaging to use DAQ boards with 12 or 14 bit resolution. However, a 12 bit DAQ board with at least 5 MS/s requires use of a computer's PCI slot and are typically 12" x 4" (Signatec PDA14). In addition, a 12 bit board at 5 MS/s generates 10Mb/s of raw data. There are USB powered DAQ boards with dimensions roughly 7" x 4" (NI USB-5132) with 8 bit resolution at 50 MS/s. With regards to a miniature OFDR needle guidance system, this is important because miniature DAQ systems often have reduced bit-depths in order to achieve adequate acquisition rates. While there is no fundamental size limitation on higher bit-depth DAQ boards, commercial considerations often require increased functionality for higher bit-depth boards. This adds cost, size, and complexity and makes higher bit-depth boards less suitable for POC OFDR systems. Even as commercially available DAQ technology improves, it is likely that 8-bit boards will always be faster and smaller than a comparable 12 or 14-bit version.

We have therefore investigated whether 8-bit sampling can be used without inhibiting image quality. In order to reduce the data transfer demand, a lower bit-depth DAQ could be used. However, the trade offs between sensitivity, dynamic range, and bit-depth have not been thoroughly investigated, making it difficult to justify and or evaluate reduced bit-depth systems. Prior analyses of the sensitivity of Fourier domain OCT systems typically assume the system is designed such that DAQ noise terms can be ignored [44, 45], or have explicitly stated that the quantization noise is minimized by the choice of detector gain [36]. Previously it has been suggested that high bit-depth DAQ boards are required for imaging through scattering tissue with high dynamic range [65]. Some groups have used 8-bit digitization for faster acquisition and lower cost and achieved a 52 dB dynamic range [66]. Huber et. al. also used an 8-bit oscilloscope at 5GS/s in order to compare 8 and 14 bit-depth images [67]. They achieved an image contrast of 37 dB in the 8 bit image, but a formal noise analysis was not presented. Here, we present a formal noise analysis of an OFDI system including the effects of bit-depth on signal quantization noise. We digitize OFDI signals at various bit-depths to analyze the effect on sensitivity and dynamic range, and compare these results with a theoretical model of OFDI that includes quantization noise. Our results show that a true 8-bit data acquisition system can achieve high system sensitivity and dynamic range with only a minimal drop in the signal-to-noise ratio. *In vivo* images of a human coronary demonstrate no significant differences between images acquired at 8- and 14-bits suggesting that 8-bit DAQ boards can be used to increase imaging speeds in clinical OFDI systems and reduce the form factor for POC applications.

5.2 Principles

In order to understand the impact of reduced bit-depth acquisition on OFDI image quality, the following set of experiments were conducted. First, a full treatment of the non-quantization dependent noise terms in OFDI including optical, electrical, and DAQ noise was developed, modified from prior works [36,44–46,68] to include quantization noise. These noise terms were then experimentally confirmed using an high bit-depth OFDI system in our laboratory. Quantization noise was then added to the model to determine a theoretical SNR as a function of bit-depth. Experimental results were obtained to model and experimentally measure the system SNR, dynamic range, and sensitivity using a high bit-depth acquisition system, for which quantization noise was minimal and could be ignored. Using these results as a baseline, the experimental data were reprocessed at various bit-depths by condensing the number of quantization levels in software and then evaluating the resulting SNR, dynamic range, and sensitivity. Because the other noise terms are analog in origin, changes in these parameters were predominantly attributed to quantization noise and the effects of reduced bit-depth acquisition. The analog noise terms were then added to a theoretical model for quantization noise to determine a theoretical SNR as a function of bit-depth. We then confirmed broad agreement between the theoretical predictions and empirical measures of image quality as a function of bit-depth.

For this analysis, we characterized the system performance using the measured SNR from a calibrated reflector in the sample arm. The SNR was measured as the ratio between the peak of the signal point spread function to the average noise floor [36, 51, 69]. The average noise floor was calculated in a region where there was no signal component. Averaging flattened the noise floor by 0.4 dB. Alternate definitions of the SNR use the mean plus the standard deviation of the noise floor [48, 49]. When the system noise is primarily set by the reference arm and not signal arm dependent, the SNR is proportional to the signal arm power. Thus, as long as this condition was preserved, the highest observed SNR served as a lower bound on the system's dynamic range. The system sensitivity was calculated from the measured SNR and the known reflectivity of the sample.

5.3 Noise analysis

5.3.1 OFDI noise

Several groups have analyzed the noise in OFDI and have shown the sensitivity advantage of Fourier domain techniques over time-domain OCT [36, 44–46]. The noise analysis and experimental method used in this paper follows the treatment found in Chen et. al [68], that describes the effect of spectrally balanced detection for OCT data acquisition. The detected current signal in OFDI is given by

$$I = I_{ref} + I_{sam} + 2 * \sqrt{I_{ref} * I_{sam}} \cos 2kz \tag{5.1}$$

Three noise sources dominate in OFDI: thermal/electrical, shot noise, and relative intensity noise (RIN). Each term is often written in units of A^2/Hz and the total noise given as

$$\sigma_n^2 = \sigma_{th}^2 + \sigma_{shot}^2 + \sigma_{RIN}^2 \tag{5.2}$$

The thermal/electrical noise comes from the detector and, in general, is not signal dependent. Shot noise arises from the statistical nature of photons and is given by

$$\sigma_{shot}^2 = 2e(\frac{\eta e}{h\nu})(P_{ref} + P_{sam}) \tag{5.3}$$

where e is the electrical charge, η the quantum efficiency of the detector, h Plank's constant, and ν the frequency of the laser light. The RIN noise is due to fluctuations in the laser power:

$$\sigma_{RIN}^2 = (\frac{\eta e}{h\nu})^2 \tau_{coh}(P_{ref} + P_{sam})^2 \tag{5.4}$$

where τ_{coh} is the coherence function of the laser. Lasers with narrow instantaneous line widths generally have larger RIN compared with more broadband lasers.

Two additional noise terms are present in OFDI, DAQ noise and quantization noise. DAQ noise is a function of the maximum voltage on the DAQ board but is not dependent on the electrical input signal. Typically, noise figures for DAQ boards are listed as a fraction of the least significant bit (LSB) and result from electronic noise within the DAQ circuitry. As the maximum allowable voltage range (V_{max}) of the DAQ increases, the voltage of the LSB increases and the absolute noise value increases proportionally. In most systems, the thermal and DAQ noise terms are much smaller than the other noise terms. With the reference power much higher than the reflected power from the sample arm ($P_{ref} >> P_{sam}$), the system can approach a shot noise limited sensitivity given by

$$\text{Sensitivity[dB]} = -10\log\left(\frac{\eta P_{sam}}{h\nu f_A}\right) \tag{5.5}$$

5.3.2 Quantization noise

Quantization noise is induced through distortions caused by the finite bit-depth of the DAQ board. Upon digitization, the analog signal is converted to a digital signal with a finite bit-depth. The number of distinct quantization levels is given by 2^b where b is the number of bits in the DAQ. The spacing of these levels is determined by the full scale voltage range and given by

$$\Delta = \frac{V_{max}}{2^b} \tag{5.6}$$

The process of quantization introduces a detection error that is often modeled as additive noise to the noise terms discussed above [70]. Quantization noise is frequently modeled as white noise with a power spectral density given by

$$\sigma_{qn}^2 = \frac{\Delta^2}{12} \tag{5.7}$$

The spectral noise density can be calculated by dividing the total quantization noise power by the detection bandwidth. This model is valid when the quantization noise is uncorrelated with the input sequence and the error probability density function is uniform over the quantization range. In addition, the model of quantization error is suitable for quasi-random input signals which are large relative to the LSB. The model breaks down, however, for small signals when the amplitude of the signal does not cross several quantization levels from sample to sample [70].

5.4 Experiments

5.4.1 OFDI System

The OFDI system used in this analysis was used in [41] and described in [15,36,40]. Briefly, the source consisted of a 40 kHz wavelength swept laser with 143 nm tuning range and an 0.156 nm instantaneous line width. Light from the laser was split into a reference and sample arm and recombined and detected using a polarization diverse receiver. An acousto-optic frequency shifter was incorporated into the reference arm to extend the ranging depth [71].

Each channel of the polarization diverse receiver was detected with a dual-balanced detector (ThorLabs PDB110C) and sampled at 85 MS/s with 14-bit resolution (Signatec PDA14) such that there with 2048 samples/A-line. A schematic of the system is shown in Fig. 5-1. The analysis below follows the noise for only one channel of the polarization diverse detection.

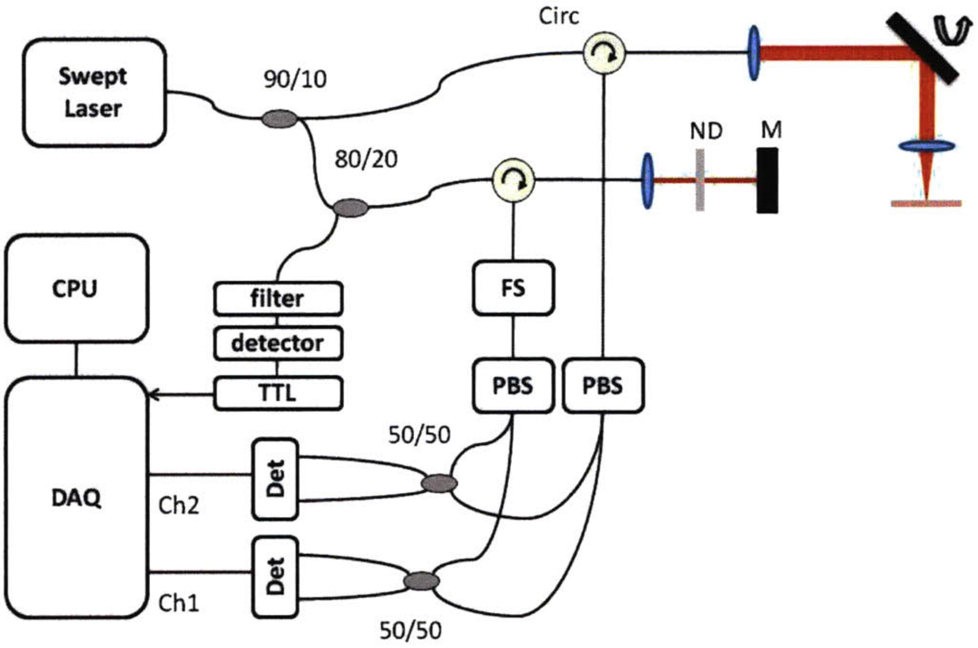

Figure 5-1: OFDI system schematic. The output of a wavelength swept laser was directed to sample and reference arms via a 90/10 coupler. The sample arm consisted of a bench top galvanometer scanner for fixed sample imaging. The reference comprised an ND filter and a fixed mirror as well as an 80/20 coupler to generate a TTL pulse for DAQ board triggering. The reference arm contained a frequency shifter (FS). Both reference and sample arms contained free space polarization beam splitters (PBS). The arms were recombined with 50/50 couplers and sent to two dual balanced receivers.

5.4.2 Noise measurements

The individual noise terms discussed above were measured as follows. First, the DAQ and thermal noise of the detector were measured by blocking both the reference and sample arms. The DAQ noise was measured by terminating the DAQ input at 50Ω and digitizing the signal with three values of V_{max} (3V, 1.6V, 1V). The thermal noise was then determined by digitizing the signal from the detector (Thorlabs PDB110C) while the optical signals were blocked, and subtracting the DAQ noise component. The results are shown in Fig. 5-2. All noise values were converted to $10 * \log_{10}(\text{pA}^2/\text{Hz})$ so that they could be compared with the optical shot and RIN noise terms. It can be seen that the thermal noise of the detector was roughly 10-20 dB greater than the DAQ noise for all values of V_{max}. The average thermal noise between 15 and 25 MHz was 3.6 pA/$\sqrt{\text{Hz}}$ which compares very well with the manufacturer's detector specification of 3.8 pA/$\sqrt{\text{Hz}}$. The theoretical quantization noise at 3V V_{max} was -8.5 pA^2/Hz which was nearly 10 dB lower than the measured DAQ noise. This trend held true for all values of V_{max}. Hence, the quantization noise was ignored. The spikes in the DAQ noise measurements were fixed pattern noise of unknown origin. We suspect they are the result of aliased harmonics of the sampling frequency as no signal was input on the DAQ during these measurements.

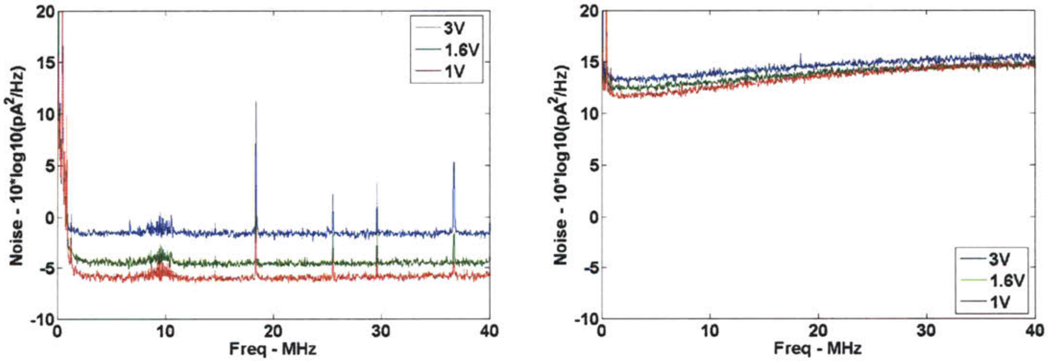

(a)

(b)

Figure 5-2: DAQ noise (left) and DAQ plus thermal noise (right) measurements at 3,1.6, and 1V V_{max}. Noise values are shown in units of $10 * \log_{10}(\text{pA}^2/\text{Hz})$.

Next the shot and RIN noise terms were measured by keeping the sample arm blocked and varying the reference arm power with a series of neutral density (ND) filters. After digitization, the DAQ and thermal noise terms were subtracted and the remaining noise was fit to the following equation

$$\sigma_n^2 = \gamma 2e\left(\frac{\eta e}{h\nu}\right)P_{ref} + P_{RIN}\left(\frac{\eta e}{h\nu}^2\right)(P_{ref})^2 \tag{5.8}$$

Here P_{RIN} is a fit factor that represents both the coherence function of the laser and the dual-balanced RIN noise reduction and γ is a correction factor that accounts for differences in the detector's quantum efficiency used in the fit and aliasing effects. The result of the fit is shown in Fig. 5-3 with γ equal to 0.83 and P_{RIN} equal to 2.48E-15. The fit and the experimental result match very well for reference powers ranging from 20 to 180 μW. Quantization noise was not included in this fit because the data was digitized at 14 bits and the quantization noise was small relative to the shot and RIN noise terms.

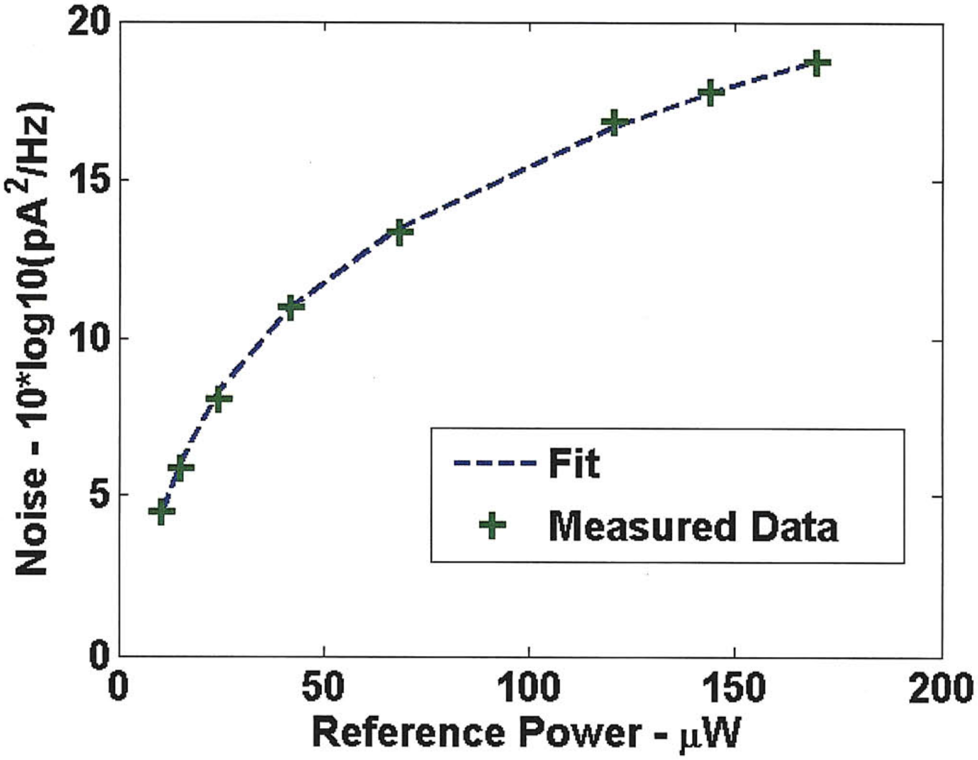

Figure 5-3: Shot plus RIN noise as a function of reference arm power. The dashed line is the fit to Eq. 5.8 with γ equal to 0.83 and P_{RIN} equal to 2.48E-15. Measured data points are shown as green crosses. Noise is displayed in units of $10 * \log_{10}(\text{pA}^2/\text{Hz})$.

5.4.3 Bit-depth reduction

With the optical and electrical noise terms well characterized, we proceeded to analyze the effect of quantization noise as a function of bit-depth. The sample arm light was directed to a fixed mirror near the zero delay point. The reference arm power was set at 17.5 μW per channel on the dual balanced receiver, which maximized the sensitivity [36]. The sample arm power was controlled using a series of ND filters. For each measurement, a background signal was collected by blocking the sample arm. After digitization, the background signal was subtracted, the signal was frequency shifted, interpolated, and Fourier transformed to assess the SNR [55].

SNR was evaluated at bit-depths ranging from the original 14 bit acquisition down to 6 bits in 1 bit increments as follows. The original data from the DAQ board was read out as an index value ranging from 1 to 2^{14}. The index value was converted to a voltage using the known V_{max} and Δ quantization spacing for 14 bits. For each bit level, a new Δ was calculated and a resampled voltage was generated using

$$V^{'} = \lfloor V/\Delta_b \rfloor * \Delta_b \tag{5.9}$$

where $\lfloor\rfloor$ represents the floor function and Δ_b the Δ at each bit depth. This transformation was performed on both the background and signal measurements prior to analysis. Alternatively, this process can be thought of as condensing the 2^{14} quantization levels into 2^b levels using

$$\text{Index}^{'} = \text{Index} - \text{rem}(\text{Index}/\text{bitRatio}) \tag{5.10}$$

where the bitRatio $= 2^{14}/2^b$.

Four data sets at different sample arm attenuations were collected and the V_{max} was set at 1V for all the data shown in Fig. 5-4. A series of 512 A-lines were collected for each sample arm attenuation and the SNR was measured at varying bit-depths. The numbers above each data set give the total attenuation in dB (44.3 dB corresponded to a sample arm power of 0.28 μW at the receiver). The maximum measured sensitivity was 106.9, 107.0, 107.2 and 105.3 dB for the four data sets respectively. Over the entire range of sample arm attenuation values, the noise was dominated by the reference arm power and the SNR was proportional to the sample arm power. Therefore, a lower bound on the system dynamic range was 63.6 dB at 14 bits and 63.0 dB at 8 bits. At higher values of V_{max} the quantization noise increased and the SNR attenuation with bit depth was more pronounced. For instance, the SNR was 63.3 dB at 14 bits and 59.9 dB at 8 bits for a V_{max} of 3V. However, assuming no other noise sources changed, adjusting the gain on the detector by a factor of 3 would make the quantization noise equal for 3V and 1V V_{max} cases such that the SNR rolloff would be identical to that shown in Fig. 5-4.

Overall, there was a high degree of correlation between the model and experimental measurements (r=0.9986). However, we observed discrepancies between the model and measurement at high bit-depths and at low bit-depths. The discrepancy at high bit depths was most pronounced for high values of attenuation. This effect may be due to the decreased accuracy of interpolation at the corresponding low values of SNR. We attribute the discrepancy at low bit depths to a breakdown in the validity of the quantization noise model when the signal no longer crosses multiple quantization levels from sample to sample. This would lead to an overestimate of the quantization noise and an underestimate of the SNR. This effect is more pronounced at higher values of V_{max} where the quantization levels are farther apart. Figure 5-5 shows the SNR loss as a function of bit-depth for each data set. At 8 bits, the loss was ~0.6 dB. The maximum observed loss was 5.5 dB at 6 bits at a

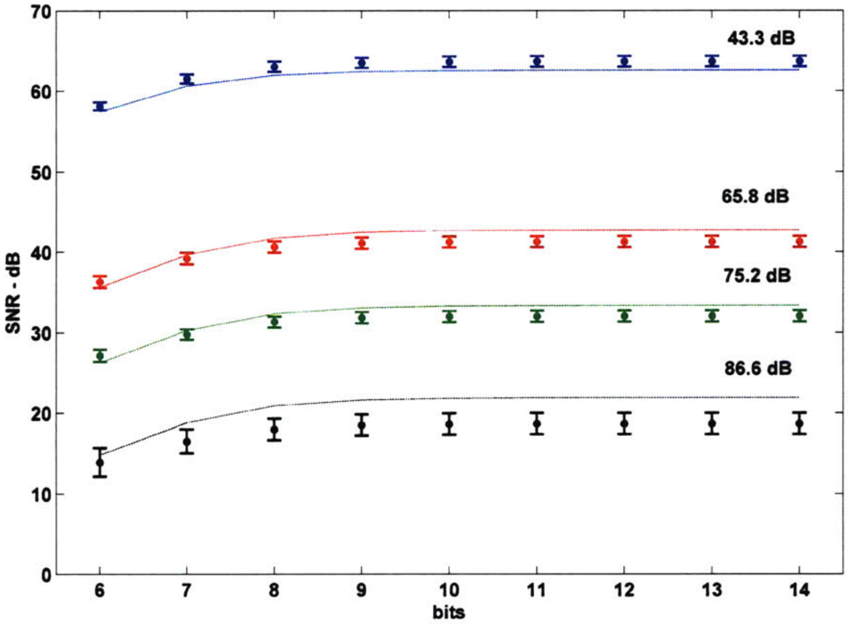

Figure 5-4: SNR as a function of bit-depth from 6 to 14 bits at four sample arm attenuation levels (44.3, 65.8, 75.2, 86.6 dB) and a 1V V_{max}. Dashed lines are theoretical SNR values using the measured shot, RIN, thermal, and DAQ noises along with the quantization noise model. Measured values are shown as closed circles with error bars representing the standard deviation.

sample arm attenuation of 43.3 dB.

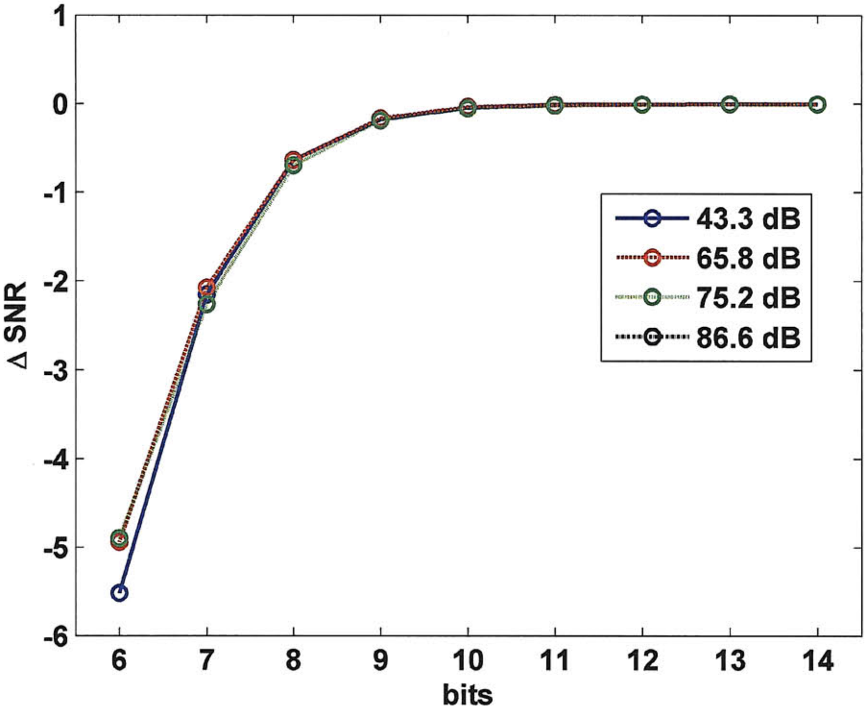

Figure 5-5: Change in SNR as a function of bit-depth. The same sample arm attenuation values are used as in Fig. 5-4. The curves overlap up to 8 bits and cannot be distinguished. The SNR loss at 8 bits for all curves is ~0.6 dB

5.5 *In vivo* imaging

In order to test whether a reduced bit-depth acquisition would be sufficient for high quality OFDI images, we reprocessed a data set from a prior human coronary artery imaging study conducted by our laboratory [42]. In this study, the OFDI data was digitized natively at 14 bits. Each A-line was bit-depth reduced in the manner described above. Figure 5-6 shows a sample frame. The images are displayed in 8-bit grayscale, but all of the numerical analysis was done on the full 14 or 8-bit data. A calcific nodule (arrow) can be seen in the lower right hand corner of the image. Even though the image dynamic range was high, there was little, if any, observable qualitative difference between the two images. Following image normalization, the root mean squared error (RMSE) difference between the two images was 2.4 dB and the mean absolute error was 1.7 dB which is in good agreement with the noise model and the experimental results from a single reflector. This error is likely to be negligible for both qualitative assessment and quantitative analysis.

A second reprocessed frame is shown in Fig. 5-7. This frame was chosen because it contained stent struts, which are metal and have a very high reflectivity. The reflectivity from the struts should provide an upper bound on the dynamic range that an OFDI system will encounter. Following image normalization, the RMSE difference between the two images was 2.3 dB and the mean absolute error was 1.5 dB indicating that reduced bit-depth images can still achieve high dynamic range.

5.6 Implications for OFDI

At increasingly higher OFDI imaging speeds, data transfer and data management demands become a limiting factor when building clinical imaging systems with the highest frame rates. In this chapter, we analyzed the system SNR, sensitivity, and dynamic range as a function of acquisition bit-depth. We compared experimental results of the SNR from a fixed reflector to an OFDI noise model that included optical, electrical, and quantization noise terms. We showed that at 8 bits the experimental loss is approximately 0.6 dB which is in good agreement with the theory. Based on our experience, if the system's sensitivity exceeds 105 dB, then this loss may be considered to be minimal. We also reprocessed OFDI frames from a human coronary artery imaging study and showed that the qualitative assessment and quantitative analysis of image quality at 8-bit was high.

Achieving good image quality at 8-bits has important implications for higher speed OFDI

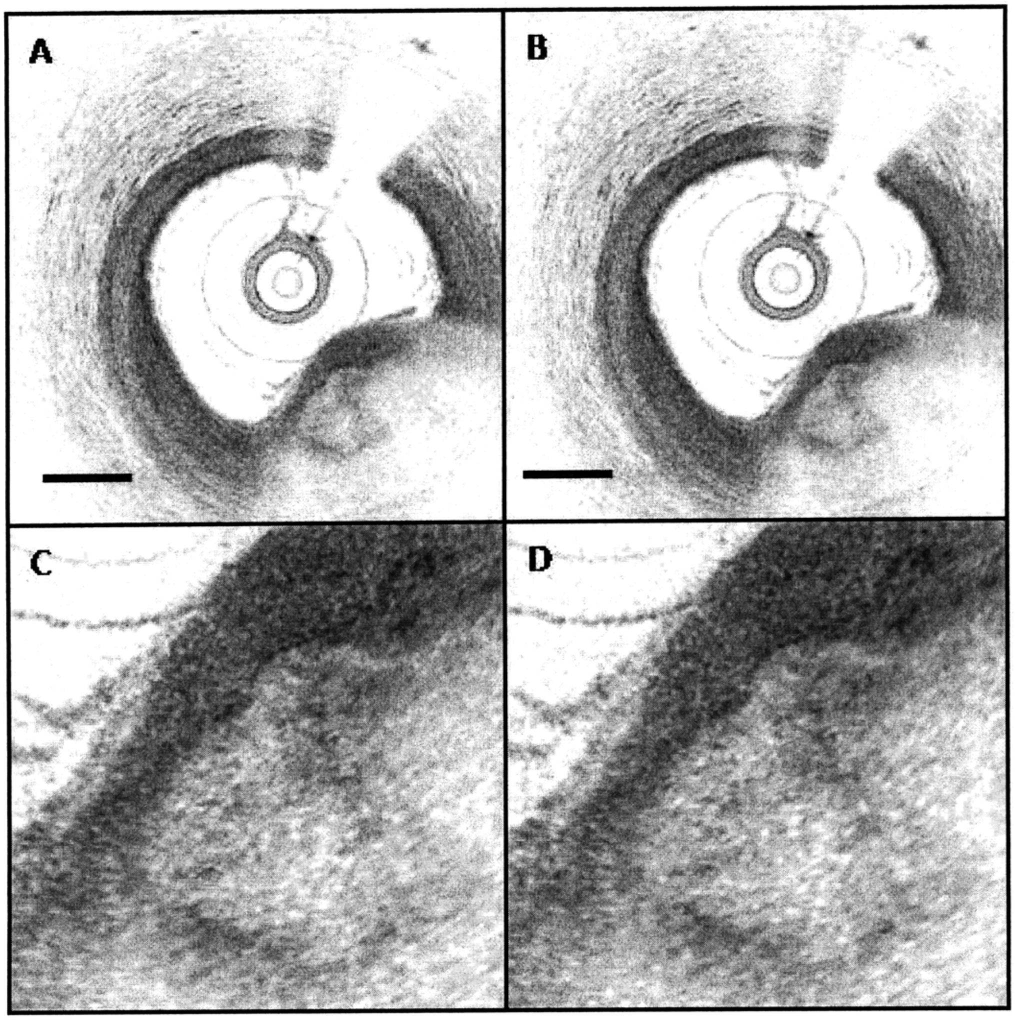

Figure 5-6: Images from a human coronary acquired *in vivo* showing a calcific nodule (arrow). (A) Original (14 bit) data. (B) Reprocessed (8 bit) data. Scale bar, 500 µm. (C) and (D) Zoomed in portion of the calcific nodule.

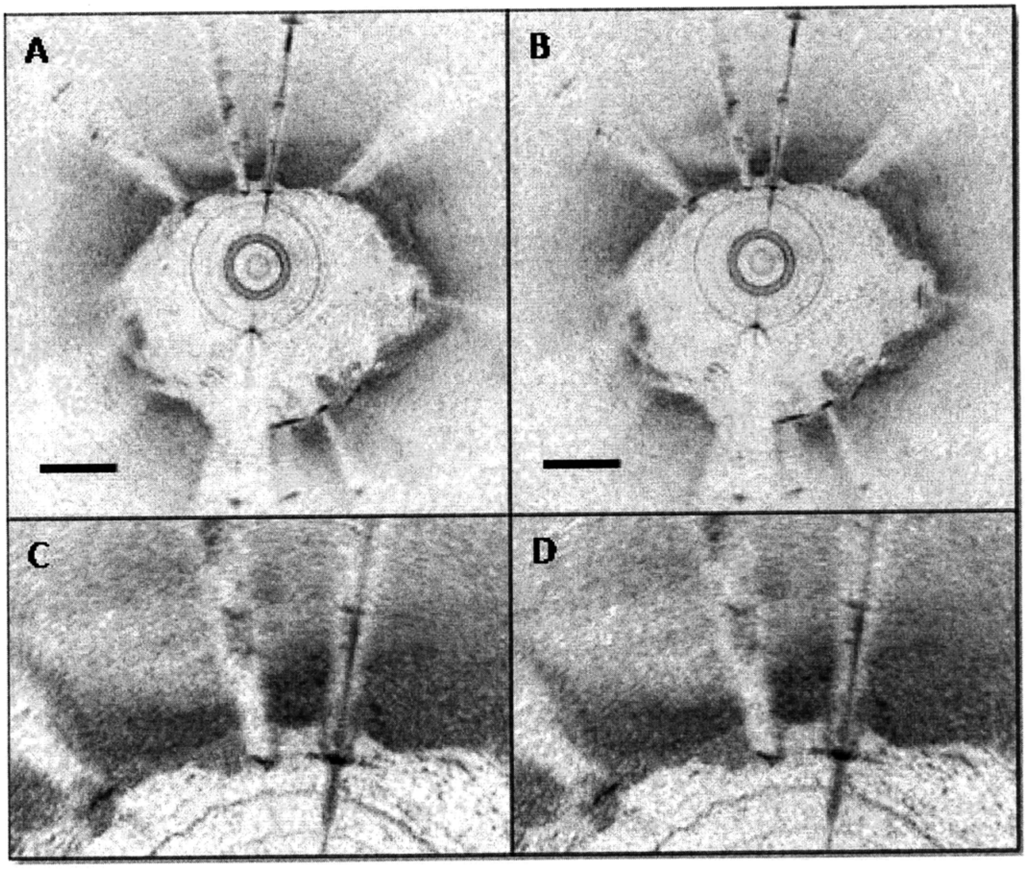

Figure 5-7: Images from a human coronary acquired *in vivo* showing a highly reflective metal stent. (A) Original (14 bit) data. (B) Reprocessed (8 bit) data. Scale bar, 500 µm. (C) and (D) Zoomed in section highlighting the high reflection metal stent.

systems, as there are 8-bit DAQ boards capable of sampling at rates of 2 GHz (GageApplied Cobra) that are commercially available. Increased sampling rates allow for increased A-line rates in OFDI imaging. Another possible use of increased sampling speed is to eliminate the need for interpolation into k-space prior to Fourier transform in the image analysis. If the sampling rate was fast enough, even sampling in k-space could be accomplished by picking out a predetermined set of data points without the need for interpolation. It is our experience that these interpolation steps take roughly half to three-quarters of the processing time and increased sampling rates could thereby speed processing rates. More analysis is needed to determine the sampling rates necessary to achieve evenly spaced k-space values for a given laser configuration and is beyond the scope of this paper. This can also be accomplished by using a swept laser that is linear in k-space [72]. In addition, reducing the acquisition bit-depth can lower the data transfer demands for an equivalent speed OFDI at higher bit-depth.

A reduction in acquisition bit-depth can be accomplished in various ways with different trade offs. Some commercially available DAQ cards such as the Signatec board used in this study allow for data to be digitized at high bit depth, followed by removal of the low order bits in firmware prior to transfer across the peripheral component interconnect (PCI) bus. Therefore these boards can generate true 8-bit data which could allow for a doubling of the A-line rate or a reduction by half of the data management demand at the same A-line rate. These boards have sampling rates in the 100-200 MS/s range.

In order to achieve an order of magnitude increase in the sampling rate to the GHz range, most commercially available DAQ boards have 8-bit maximum bit-depths. However, with all DAQ boards, the more important number is the effective number of bits (ENOB). The ENOB indicates that the DAQ is equivalent to an ideal DAQ with the corresponding ENOB.

The ENOB is calculated by measuring the signal to noise and distortion ratio (SINAD) which is the ratio of the signal amplitude to the sum of all other spectral components including harmonics. The ENOB is then calculated as ENOB = (SINAD - 1.76)/6.02 [73]. For an 8-bit board, the ENOB can be as high as 7.4 bits at sampling rates of 1 or 2 GHz (GageApplied Cobra). This will increase the SNR loss by between 0-1 dB. In addition, the shot noise limited sensitivity is reduced at higher A-line rates as seen in Eq. 5.5. This drop in sensitivity can be overcome by increasing the sample arm power. Other high-speed DAQ boards in the GHz range can digitize at 10-bits with an ENOB as high as 7.8 at 1.7 Gs/s (Pentek 6826002P). In order to overcome the word length constraint of most computers, these boards would need to either drop the low order bits in firmware or be used with custom field-programmable gate array processors with variable word lengths. There may be other factors that affect a hardware based reduction in bit-depth such as offset, non-linearity, and gain error. We don't anticipate this to be a major issue because these errors are often less than one LSB.

We have shown that intensity based OFDI images do not suffer from reduced image quality at 8-bits compared with 14-bit acquisition. One limitation of this technique is that phase based measurements such as polarization or Doppler techniques may suffer from additional loss. However, the sensitivity of Doppler measurements are related to $\sqrt{SNR}$ such that the loss could be minimized [74].

In addition, V_{max} was selected to match the maximum expected voltage range of the OFDI signal. This reduces the quantization noise to its lowest level while still maintaining high dynamic range. In tissue imaging, the maximum signal is not known a priori and a highly backscattering signal could in principle exceed V_{max}. As discussed above, increasing V_{max} will increase the quantization noise and introduce higher SNR loss at decreased bit-depth. We do not believe this to be a major limitation because high quality OFDI images rarely exceed 50 dB of dynamic range and we have demonstrated that at least 63.0 dB of dynamic range at 8-bits is achievable.

Chapter 6

Discussion

Chapters 3, 4, and 5 discussed enabling technologies for building a point-of-care (POC) optical technology for integrated guidance of fine needle aspiration breast biopsy (FNAB) and chapter 2 laid out design criteria for a successful POC technology. The technologies presented in the previous chapters all contain elements of these design criteria. The following chapter will summarize each component and discuss the pros and cons of each technology with respect to POC design criteria as well as the necessary steps for integrating each component into a fully portable system.

6.1 POC Design Criteria

6.1.1 Automated Algorithm

FNAB suffer from high non-diagnostic sampling rates and and would benefit from an integrated needle guidance technique that could differentiate tissue types. We have developed an automated algorithm for differentiating ex vivo adipose tissue and fibroglandular human breast tissue using low coherence interferometry that achieves a high sensitivity and specificity. This is important because the majority of non-diagnostic samples in FNAB are from adipose tissue. The ability to identify adipose tissue in real-time at the tip of the biopsy needle would allow the clinician to move the biopsy needle to a better location and improve sample yield. With respect to the POC design criteria, the algorithm is simple and easy to use as it is automatic and requires no additional input from the end user; the algorithm is accurate with high sensitivity and specificity; and the algorithm is robust with low intra-sample variability.

We have shown that in our model, tumor samples are correctly classified as fibroglandular suggesting that they won't be misclassified as adipose tissue, resulting in a missed diagnosis. In order to subclassify tumor tissues or add additional tissue types such as necrotic tissue to the classification algorithm more sophisticated models may be required. However, in order to be useful in a POC setting, the classification must be done in real time in order to provide immediate feedback to the clinician; fast computation should always be kept as a design criteria when analyzing the overall improvement in the classification result. The extracted parameters used for classification are simple and require minimal additional computation time compared with the standard post-processing of the LCI signals. In addition, the classification model is simple, and requires minimal computation. More sophisticated classification models such as neural networks, decision trees, or models that extract more signal parameters may improve overall classification statistics, but could come at the cost of increased computation time and loss of real-time analysis.

6.1.2 Miniature Source

One of the most important design criteria for a POC FNAB technology is size and portability. The LCI system used in the previous algorithm study was briefcase sized and not suitable for hand-held clinical use. In addition, the A-line rate of the LCI system was slow and left it susceptible to motion artifacts and an inability to generate two-dimensional images at video-rate.

In order to overcome these limitations we have built a novel miniature wavelength-swept laser suitable for point-of-care OFDR or OFDI. The system can be fully battery powered, has a small footprint, and achieves a peak output power of 12 mW, 75 nm tuning bandwidth, and 0.24 nm instantaneous linewidth. Wavelength tuning is accomplished by using a reflection grating and a miniature resonant scanning mirror rotating at 15.3 kHz. At this A-line rate, video-rate images can be achieved with 512 lines/frame. Utilizing both forward and backward wavelength sweeps enables OFDI imaging at 30.6 kHz A-line rates which can be used to double the frame rate, or employed to reduce speckle noise (Fig. 4-9).

The overall size of the miniature laser is very small and could be used in a hand-held OFDR system. The optical footprint is roughly the size of a deck of cards (Fig. 4-1). In addition, the laser can be battery powered for over an hour which is more than sufficient for FNAB procedures. Together, the commercially available laser driver, temperature controller, and resonant scanner drivers would fit into a package roughly the size of 2-3 decks of cards including the batteries that drive each component. Therefore, the miniature laser fulfills both the small size, and high portability design criteria for successful POC technologies.

6.1.3 Reduced Bit-Depth Acquisition

At increasingly higher OFDI imaging speeds, data transfer and data management demands become a limiting factor when building clinical imaging systems with the highest frame rates. Even in POC systems where the data demands may be reduced, size and simplicity of the data acquisition and computer electronics is an important design criteria. We have investigated the use of reduced bit-depth data acquisition for OFDI and shown that signal SNR, dynamic range, and sensitivity can be maintained at high levels. The ability to digitize at reduced bit-depths can reduce the data transfer and data management demands as well as reduce the form factor needed for an appropriate DAQ card.

The design of a custom built DAQ board is outside the scope of this thesis. However, it is important to outline the necessary design parameters for such a DAQ that could be used with the miniature swept source in a portable OFDR system. The miniature source has a repetition rate of 15.3 kHz. However, because the wavelength swept source is bidirectional, the effective repetition rate is 30.6 kHz. The minimum number of points per A-line is given by $2 * \Delta\lambda/\delta\lambda$. Therefore, only 625 points per A-line are needed and a sampling rate of ~20 Ms/sec is required. However, in order to avoid avoid limitations in the ranging depth due to fringe washout [51], the sampling rate is often increased. In this case, 40 Ms/sec would probably be sufficient.

At the detection end, only one dual-balanced receiver is required for a non-polarization diverse OFDR system. Therefore, only one analog input on the DAQ is required. A second analog input would allow for polarization diverse or polarization sensitive measurements. A third input is needed to add phase-sensitive Doppler flow measurements in order to detect the calibration signal [75]. Also, a 5V TTL signal is generated from the resonant scanner drive circuity. An analog or digital input is needed for this signal to serve as the acquisition trigger. No analog or digital output is needed if only one-dimensional signals from the forward looking sample probe are used. However, if imaging is required, the optical fiber would need to be rotated or moved in some manner and a portable imaging system would require distal optics such as MEMS based scanners to generate an image. To drive these additional components, an analog output would most likely be required.

Another important design criteria is size. The actual physical size of the laser optics was approximately 3 in. x 2.5 in. x 3 in. Ideally, a custom DAQ would fit in this general form factor. A summary of these design parameters is listed in table 6.1.

Table 6.1: DAQ design criteria for POC FNAB guidance.

Parameter	Minimum	Ideal
Sampling rate (Ms/sec)	20	40
Analog inputs	1	2 or 3
Digital inputs	0	1
Analog outputs	0	1
Size	4 in. x 6 in.	3 in. x 2.5 in.

6.1.4 Additional Design Elements

The clinical probe is an additional design element that is the subject of ongoing investigation. A clinical POC system for FNAB would require the ability to collect tissue aspirates directly following the OFDR measurement. The probe should also be disposable and inexpensive. The current probe fits within the POC design criteria because it is small, fits within current standard FNAB needles, and is very inexpensive. Due to the high demand of optical fiber in telecommunications, a one meter patch cord of optical fiber would cost only a few cents. The connector to attach the probe to the OFDR system costs on the order of a few dollars such that a complete probe would be less than $5.

In order to collect the tissue aspirate either simultaneously, or directly following the OFDR measurement, a number of designs have been proposed. The basic design of the integrated optical fiber/needle probe involves protecting and securing the optical fiber within a separate lumen from the needle bore where the aspirate is collected. Figure 6-1 shows one implementation where the separate lumen runs within the wall thickness of a standard

FNAB needle. The dimensions are given for a custom needle that combines the dimensions of the 23 and 25 needles used in FNA procedures. The OD is 635 μm and the ID is 241 μm which makes the wall thickness of the needle 197 μm. A 125 μm optical fiber could then fit within a separate lumen that runs within the wall thickness. The optical fiber would be secured with the separate lumen by the use of standard optical epoxies that can bond both metal and glass. The probe end of the optical fiber would be located along the beveled edge of the needle and optically interrogate the tissue near the tip of the needle. In addition, new advancements in optical fiber technology have made 80 μm diameter optical fiber commercially available which could further reduce the size of the needle design.

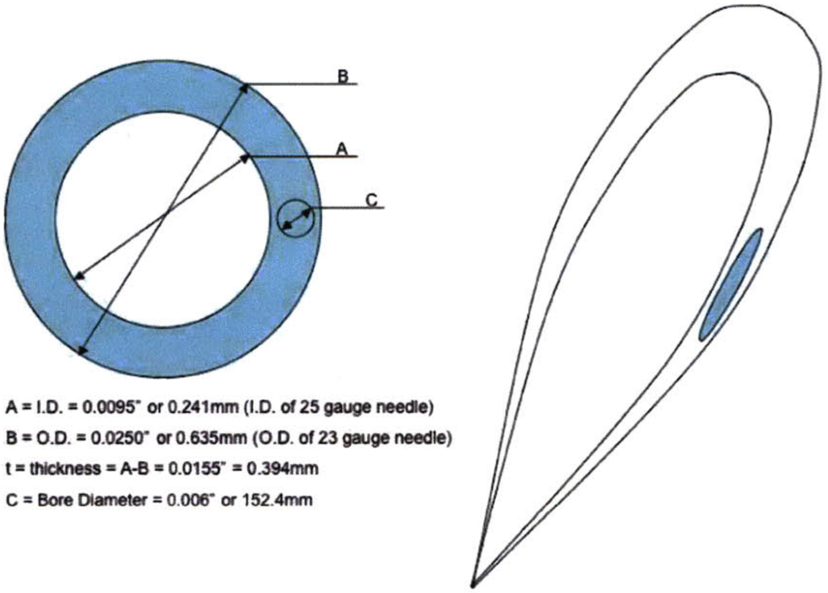
B
A
C
A = I.D. = 0.0095" or 0.241mm (I.D. of 25 gauge needle)
B = O.D. = 0.0250" or 0.635mm (O.D. of 23 gauge needle)
t = thickness = A-B = 0.0155" = 0.394mm
C = Bore Diameter = 0.006" or 152.4mm

Figure 6-1: Integrated optical fiber/needle probe design where optical fiber travel travels within a separate lumen.

The advantage of this design is that the optical fiber is completely separate from the aspiration lumen and wouldn't limit the collection of aspirates in any way. In addition, the optical fiber would be completely secured to the needle such that it would not move during advancement of the needle. The mechanical stability would prevent any bending or breakage of the fiber probe. Only the tip of the fiber probe would come in direct contact with the tissue. A similar design is to use a small hypodermic tube as the housing for the optical fiber. Hypodermic tubes are the metal tubes from which needles are made and they come in a variety of sizes. The smallest hypodermic tube that standard 125 μm fits into is 30 gauge (305 μm OD, 140 μm ID) and the new 80 μm fiber fits into 33 gauge (203 μm OD, 89 μm ID). The optical fiber could be inserted and secured with optical epoxy into the lumen of the hypodermic tubes. The tube would provide mechanical strength to the fiber and could be either inserted, or attached to the FNA needles in a variety of ways.

One implementation is shown in Fig. 6-2. The hypodermic tube is inserted directly into the lumen of the FNA needle and positioned at the tip of the needle. The hypodermic tube and fiber could be angle polished to match the beveled edge of the needle in order to perfectly match geometries of the two tubes. A disadvantage of this design is that a portion of the lumen is still taken up by the hypodermic tube and fiber which limits the usable space for aspirate collection. However, it may still be possible to collect adequate samples using this design. Another approach is to move the hypodermic tube and fiber slightly back from the needle tip in order to leave the needle cutting edge unaffected. This implementation is shown is Fig. 6-3.

A related approach is to create a custom needle that combines the two above approaches in a so called "double-lumen" design. This implementation is shown in Fig. 6-4. Here, the first lumen is the standard lumen from the FNA needle and the second lumen is the hypodermic tube which can be used for mechanical strength and protection of the fiber. Again, the hypodermic tube and fiber could be polished in such a way to match the geometry of the cutting edge of the needle. In fact, the second lumen created by the hypodermic tube

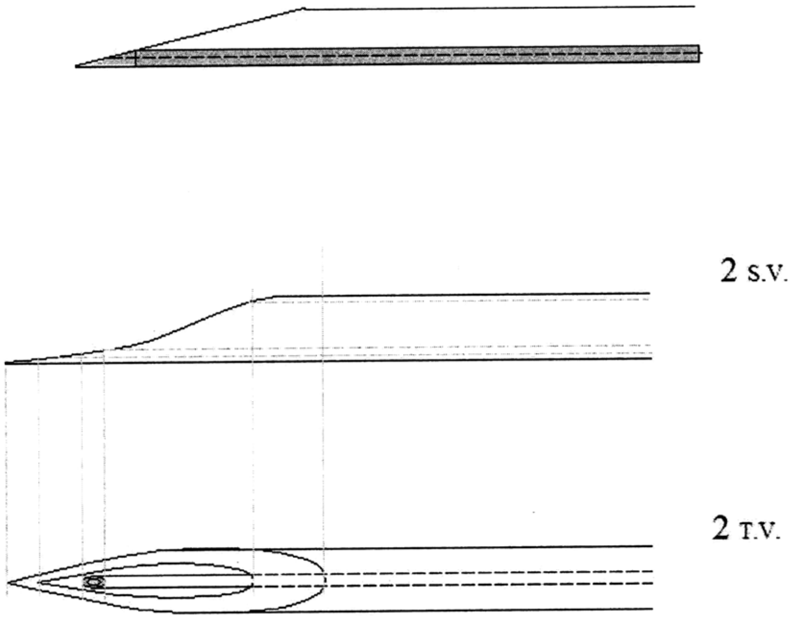

Figure 6-2: Integrated optical fiber/needle probe design with optical fiber protected within a hypodermic tube.

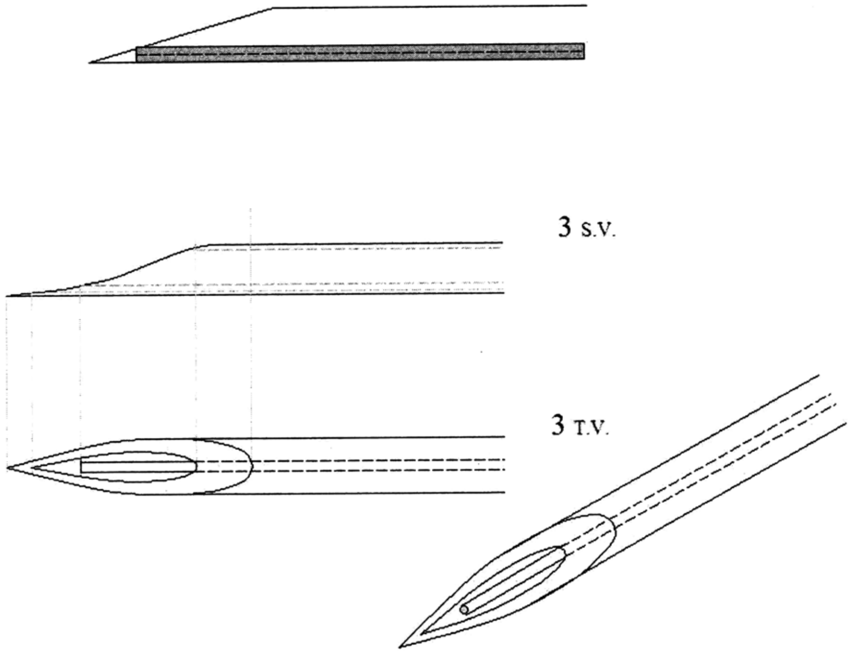

Figure 6-3: Integrated optical fiber/needle probe design with optical fiber protected within a hypodermic tube and offset from needle tip to avoid cutting edge.

could be attached to any side of the needle including the bottom, side, or top as shown in Fig. 6-5. The advantage of this design is that the wall thickness of the needle is not reduced or compromised and that complete lumen area is available for aspirate collection.

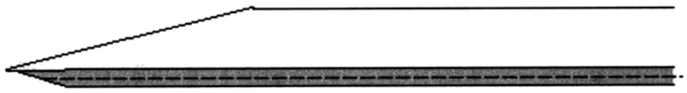

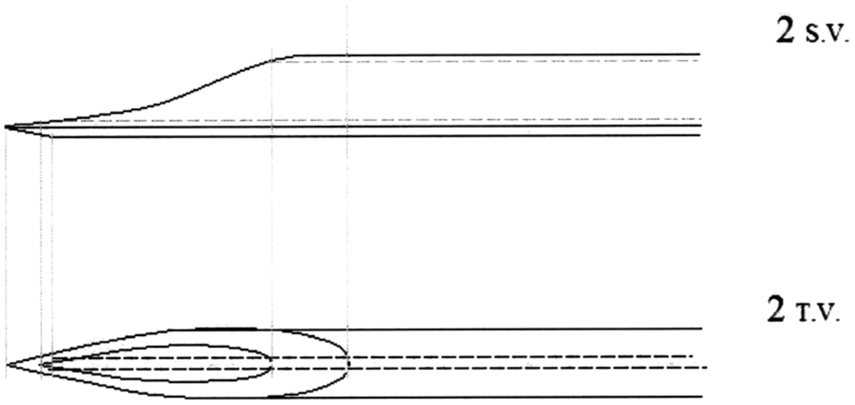

Figure 6-4: Integrated optical fiber/needle probe design with double lumen for aspirate and optical fiber.

A final implementation is to create a groove within the needle surface that houses the optical fiber. The groove would run the length of the needle and the optical fiber would be secured to the needle with medical grade epoxy. The groove can be made anywhere on the outer circumference of the needle except the tip which is used as the cutting surface. An implementation where the groove runs along the top of the needle is shown in Fig. 6-6.

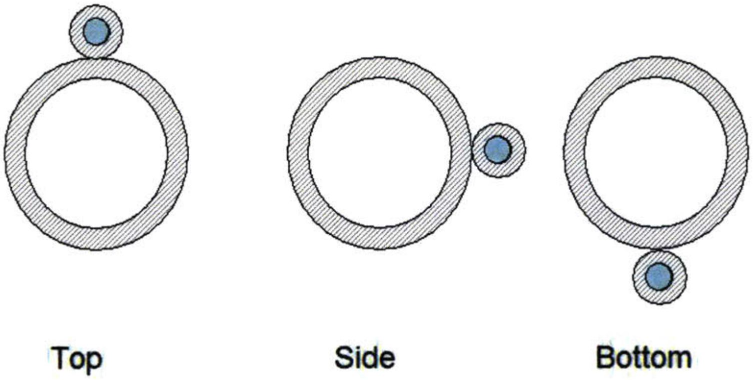

Figure 6-5: Integrated optical fiber/needle probe design with optical fiber attached to the side, top, or bottom of the needle.

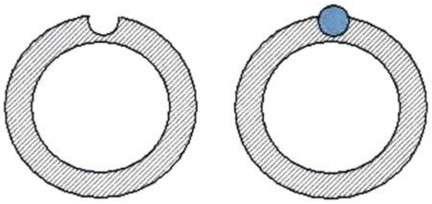

Figure 6-6: Integrated optical fiber/needle probe design with optical fiber running in a groove of the FNA needle.

6.2 Summary and Conclusion

This thesis investigated the use LCI, and its second generation OFDR, for integrated guidance of FNAB procedures and developed novel optical technologies that enable POC implementation. An automated algorithm for differentiating human breast tissue was developed with high sensitivity and specificity. The algorithm was simple, robust, and easy to implement in a real-time POC environment. In order to achieve hand-held clinical implementation of an OFDR system, a miniature, battery-powered swept laser was built. The laser is capable of video-rate imaging at A-line rates over 30 kHz and with imaging sensitivity near 100 dB. Lastly, the performance of reduced bit-depth acquisition for OFDR was studied and it was shown that 8-bit acquisition can achieve high image quality with little drop in SNR compared with higher bit-depth acquisition. This is important for reducing the data transfer and data management demands of OFDR and for reducing the form factor of DAQ systems in POC applications. While we have focused on the application of FNAB for breast pathology, these technologies can be applied in a number of different clinical settings including needle placement for vascular access and lumbar punctures. The portable nature of the miniature source may also allow OFDR and OFDI technologies to be used in field based medicine for military or third-world applications. Finally, the reduced bit-depth acquisition analysis may play an important role as large scale, high-speed OFDI systems are hampered by electronic rather than optical limitations.

THIS PAGE INTENTIONALLY LEFT BLANK

Bibliography

[1] Steven M Wright, David G. Brown, Jay R Porter, David C Spence, Emillio Esparza, David C Cole, and F. Russell Huson. A desktop magnetic resonance imaging system. *Magnetic Resonance Materials in Physics, Biology, and Medicine*, 13(3):177–185, 2001.

[2] Daniel A. Lichtenstein. Point-of-care ultrasound: Infection control in the intensive care unit. *Crit Care Med*, 35(5):S262 – S267, 2007.

[3] Dan Harvey. The incredible shrinking modality. *Radiology Today*, 7(5):18, 2006.

[4] Hans Knotzer and Walter R Hasibeder. Microcirculatory function monitoring at the bedside-a view from the intensive care. *Physiological Measurement*, 28(9):R65, 2007.

[5] L. V. Rao, Bjorn A. Ekberg, Diane Connor, Felice Jakubiak, Guy M. Vallaro, and Michael Snyder. Evaluation of a new point of care automated complete blood count (cbc) analyzer in various clinical settings. *Clinica Chimica Acta*, 389(1-2):120–125, 2008.

[6] Zhen Yang and Dao Min Zhou. Cardiac markers and their point-of-care testing for diagnosis of acute myocardial infarction. *Clinical Biochemistry*, 39(8):771–780, 2006.

[7] R. Scott Evans, Stanley L. Pestotnik, David C. Classen, Terry P. Clemmer, Lindell K. Weaver, James F. Orme, James F. Lloyd, and John P. Burke. A computer-assisted management program for antibiotics and other antiinfective agents. *N Engl J Med*, 338(4):232–238, 1998.

[8] Nancy C. Nelson, R. Scott Evans, Matthew H. Samore, and Reed M. Gardner. Detection and prevention of medication errors using real-time bedside nurse charting. *J Am Med Inform Assoc*, 12(4):390–397, 2005.

[9] Per H. Gesteland, Reed M. Gardner, Fu-Chiang Tsui, Jeremy U. Espino, Robert T. Rolfs, Brent C. James, Wendy W. Chapman, Andrew W. Moore, and Michael M. Wagner. Automated syndromic surveillance for the 2002 winter olympics. *J Am Med Inform Assoc*, 10(6):547–554, 2003.

[10] Christopher P. Price and Larry J. Kricka. Improving healthcare accessibility through point-of-care technologies. *Clin. Chem.*, 53(9):1665–1675, 2007.

[11] Yanick Beaulieu. Bedside echocardiography in the assessment of the critically ill. *Crit. Care. Med.*, 35(5):S235–S249, 2007.

[12] S Gupta and DC Madoff. Image-guided percutaneous needle biopsy in cancer diagnosis and staging. *Tech. Vasc. Interv. Radiol.*, 10(2):88–101, 2007.

[13] Adam M. Zysk and Stephen A. Boppart. Computational methods for analysis of human breast tumor tissue in optical coherence tomography images. *J. Biomed. Opt.*, 11(5), 2006.

[14] Melissa J. Suter, Benjamin J. Vakoc, Norman S. Nishioka, Patrick S. Yachimski, Milen Shishkov, Reza Motaghiannezam, Brett E. Bouma, and Guillermo J. Tearney. In vivo 3d comprehensive microscopy of the human distal esophagus. *Gastrointestinal Endoscopy*, 65(5):AB154–905, 2007.

[15] Benjamin J. Vakoc, Milen Shishko, Seok H. Yun, Wang-Yuhl Oh, Melissa J. Suter, Adrien E. Desjardins, John A. Evans, Norman S. Nishioka, Guillermo J. Tearney, and Brett E. Bouma. Comprehensive esophageal microscopy by using optical frequency-domain imaging (with video). *Gastrointestinal Endoscopy*, 65(6):898–905, 2007.

[16] John A. Evans, John M. Poneros, Brett E. Bouma, Jason Bressner, Elkan F. Halpern, Milen Shishkov, Gregory Y. Lauwers, Mari Mino-Kenudson, Norman S. Nishioka, and Guillermo J. Tearney. Optical coherence tomography to identify intramucosal carcinoma and high-grade dysplasia in barrett's esophagus. *Clinical Gastroenterology and Hepatology*, 4(1):38–43, 2006.

[17] M. A. S. Frable and W. J. Frable. Fine-needle aspiration biopsy of salivary-glands. *Laryngoscope*, 101(3):245–249, 1991.

[18] S. R. S. Mandreker, N. S. Nadkarni, R. G. W. Pinto, and S. Menezes. Role of fine-needle aspiration cytology as the initial modality in the investigation of thyroid lesions. *Acta. Cytologica*, 39(5):898–904, 1995.

[19] Susan Klein. Evaluation of palpable breast masses. *American Family Physician*, 71(9):1731–1738, 2005.

[20] E. Azavedo, G. Svane, and G. Auer. Stereotactic fine-needle biopsy in 2594 mammographically detected non-palpable lesions. *The Lancet*, 333(8646):1033–1036, 1989. TY - JOUR.

[21] Michael S Ballo and Nour Sneige. Can core needle biopsy replace fine-needle aspiration cytology in the diagnosis of palpable breast carcinoma: A comparative study of 124 women. *Cancer*, 78(4):773–777, 1996. 10.1002/(SICI)1097-0142(19960815)78:4¡773::AID-CNCR13¿3.0.CO;2-S.

[22] Catherine M. Antley, Eoghan E. Mooney, and Lester J. Layfield. A comparison of accuracy rates between open biopsy, cutting-needle biopsy, and fine-needle aspiration biopsy of the breast: A 3-year experience. *The Breast Journal*, 4(1):3–8, 1998.

[23] Nour Sneige Scott Boerner. Specimen adequacy and false-negative diagnosis rate in fine-needle aspirates of palpable breast masses. *Cancer Cytopathology*, 84(6):344–348, 1998.

[24] Rima Bakhos, Suzanne M. Selvaggi, Steven DeJong, Donald L. Gordon, Shailesh U. Pitale, Marrille Herrmann, and Eva M. Wojcik. Fine-needle aspiration of the thyroid: Rate and causes of cytohistopathologic discordance. *Diagnostic Cytopathology*, 23(4):233–237, 2000.

[25] W. H. Hindle and E. C. Chen. Accuracy of mammographic appearances after breast fine-needle aspiration. *American Journal of Obstetrics and Gynecology*, 176(6):1286–1290, 1997.

[26] Andrew Saxe, Eduardo Phillips, Pareskevi Orfanou, and Mujtaba Husain. Role of sample adequacy in fine needle aspiration biopsy of palpable breast lesions. *The American Journal of Surgery*, 182(4):369–371, 2001.

[27] Britt-Marie Ljung, Anne Drejet, Nona Chiampi, Juli Jeffrey, William H. Goodson III, Karen Chew, Dan H. Moore II, and Theodore R. Miller. Diagnostic accuracy of fine-needle aspiration biopsy is determined by physician training in sampling technique. *Cancer Cytopathology*, 93(4):263–268, 2001. 10.1002/cncr.9040.

[28] Sanjay Gupta, Karen Seaberg, Michael J. Wallace, David C. Madoff, Jr. Morello, Frank A., Kamran Ahrar, Ravi Murthy, and Marshall E. Hicks. Imaging-guided percutaneous biopsy of mediastinal lesions: Different approaches and anatomic considerations. *Radiographics*, 25(3):763–786, 2005.

[29] Peter Skippen and Niranjan Kissoon. Ultrasound guidance for central vascular access in the pediatric emergency department. *Pediatric Emergency Care*, 23(3):203–207, 2007.

[30] Xingde Li, Christian Chudoba, Tony Ko, Costas Pitris, and James G Fujimoto. Imaging needle for optical coherence tomography. *Opt. Lett.*, 25(20):1520–1522, 2000.

[31] Y. Z. Zhu and A. B. Wang. Miniature fiber-optic pressure sensor. *IEEE Photon. Technol. Lett.*, 17(2):447–449, 2005.

[32] Maureen Johns, Cole A. Giller, Dwight German, and Hanli Liu. Determination of reduced scattering coefficient of biological tissue from a needle-like probe. *Opt. Express*, 13(13):4828–4842, 2005.

[33] Adam M. Zysk, Steven G. Adie, Julian J. Armstrong, Matthew S. Leight, Alexandre Paduch, David D. Sampson, Freddy T. Nguyne, and Stephen A. Boppart. Needle-based refractive index measurement using low-coherence interferometry. *Opt. Lett.*, 32(4), 2007.

[34] William A. Reed, Man. F Yan, and Mark J. Schnitzer. Gradient-index fiber-optics microprobes for minimally invasive in vivo low-coherence interferometry. *Opt. Lett.*, 27(20):1794–1796, 2002.

[35] David Huang, Eric A. Swanson, Charles Lin, Joel S. Schuman, William Stinson, Warren Chang, Michael Hee, Thomas Flotte, Kenton Gregory, Carmen Puliafito, and J.G. Fujimoto. Optical coherence tomography. *Science*, 254:1178–1181, 1991.

[36] S.H. Yun, Guillermo J. Tearney, J.F. de Boer, N. Iftimia, and Brett E. Bouma. High-speed optical frequency-domain imaging. *Opt. Express*, 11(22):2953–2963, 2003.

[37] Nicusor V. Iftimia, Brett E. Bouma, Martha B. Pitman, Brian Goldberg, Jason Bressner, and Guillermo J. Tearney. A portable, low coherence interferometry based instrument for fine needle aspiration biopsy guidance. *Review of Scientific Instruments*, 76(6):064301, 2005.

[38] M. B. Pitman, 2007.

[39] A F Fercher, W Drexler, C K Hitzenberger, and T Lasser. Optical coherence tomography - principles and applications. *Reports on Progress in Physics*, 66(2):239–303, 2003.

[40] Seok H. Yun, Guillermo J. Tearney, Benjamin J. Vakoc, Milen Shishkov, Wang Y. Oh, Adrien E. Desjardins, Melissa J. Suter, Raymond C. Chan, John A. Evans, Ik-Kyung Jang, Norman S. Nishioka, Johannes F. de Boer, and Brett E. Bouma. Comprehensive volumetric optical microscopy in vivo. *Nat. Med.*, 12(12):1429–1433, 2007. 1078-8956 10.1038/nm1450 10.1038/nm1450.

[41] Melissa J. Suter, Benjamin J. Vakoc, Patrick S. Yachimski, Milen Shishkov, Gregory Y. Lauwers, Mari Mino-Kenudson, Brett E. Bouma, Norman S. Nishioka, and Guillermo J. Tearney. Comprehensive microscopy of the esophagus in human patients with optical frequency domain imaging. *Gastrointestinal Endoscopy*, 68(4):745–753, 2008. 0016-5107 doi: DOI: 10.1016/j.gie.2008.05.014.

[42] Guillermo J. Tearney, Sergio Waxman, Milen Shishkov, Benjamin J. Vakoc, Melissa J. Suter, Mark I. Freilich, Adrien E. Desjardins, Wang-Yul Oh, Lisa A. Bartlett, Mireille Rosenberg, and Brett E. Bouma. Three-dimensional coronary artery microscopy by intracoronary optical frequency domain imaging. *J Am Coll Cardiol Img*, 1(6):752–761, 2008.

[43] A. F. Fercher, K. Mengedoht, and W. Werner. Eye-length measurement by interferometry with partially coherent light. *Opt. Lett.*, 13(3):186–188, 1988.

[44] J.F. de Boer, B. Cense, B.H. Park, M.C. Pierce, G.J. Tearney, and B.E. Bouma. Improved signal-to-noise ratio in spectral-domain compared with time-domain optical coherence tomography. *Opt Lett*, 28:2067–2069, 2003.

[45] Michael Choma, Marinko Sarunic, Changhuei Yang, and Joseph Izatt. Sensitivity advantage of swept source and fourier domain optical coherence tomography. *Opt. Express*, 11(18):2183–2189, 2003.

[46] R. Leitgeb, C. Hitzenberger, and Adolf Fercher. Performance of fourier domain vs. time domain optical coherence tomography. *Opt. Express*, 11(8):889–894, 2003.

[47] S.H. Yun, C. Boudoux, Guillermo J. Tearney, and Brett E. Bouma. High-speed wavelength-swept semiconductor laser with a polygon-scanner-based wavelength filter. *Opt. Lett.*, 28(20):1981–3, 2003.

[48] R. Huber, M Wojtkowski, and J. G Fujimoto. Fourier domain mode locking (fdml): A new laser operating regime and applications for optical coherence tomography. *Opt. Express*, 14(8):3225–3237, 2006.

[49] Michael Choma, Kevin Hsu, and Joseph Izatt. Swept source optical coherence tomography using an all-fiber 1300-nm ring laser source. *J. Biomed. Opt.*, 10(4):044009, 2005.

[50] F. Lexer, C. K. Hitzenberger, A. F. Fercher, and M. Kulhavy. Wavelength-tuning interferometry of intraocular distances. *Appl. Opt.*, 36(25):6548–6553, 1997.

[51] S.H. Yun, G.J. Tearney, B.E. Bouma, B.H. Park, and J.F. de Boer. High-speed spectral-domain optical coherence tomography at 1.3 um. *Optics Express*, 11(26):3598–3604, 2003.

[52] J. M. Schmitt, Zhou Guan-Xiong, and Justin Miller. Measurement of blood hematocrit by dual-wavelength near-ir photoplethysmography. In *SPIE Proceedings*, volume 1641, 1992.

[53] Michael P. Stern and Fred Conrad. An automated, direct method for measuring adipocyte cell size. *Clinica Chimica Acta*, 65(1):29–37, 1975. TY - JOUR.

[54] Bernard Rosner. *Fundamentals of Biostatistics*. Duxbury, 5 edition, 2000.

[55] S. H. Yun, C. Boudoux, M. C. Pierce, J. F. de Boer, G. J. Tearney, and B. E. Bouma. Extended-cavity semiconductor wavelength-swept laser for biomedical imaging. *IEEE Photon. Technol. Lett.*, 16(1):293–295, 2004. 1041-1135.

[56] Alexandre R. Tumlinson, Jennifer K Barton, Boris Povazay, Harald Sattman, Angelika Unterhuber, Rainer A. Leitgeb, and Wolfgang Drexler. Endoscope-tip interferometer for ultrahigh resolution frequency domain optical coherence tomography in mouse colon. *Opt. Express*, 14(5):1879–1887, 2006.

[57] S. R. Chinn, E. A. Swanson, and J. G. Fujimoto. Optical coherence tomography using a frequency-tunable optical source. *Opt. Lett.*, 22(5):340–342, 1997.

[58] Chong Changho, A. Morosawa, and T. Sakai. High-speed wavelength-swept laser source with high-linearity sweep for optical coherence tomography. *IEEE J. Sel. Top. Quantum Electron.*, 14(1):235–242, 2008. 1077-260X.

[59] S. W. Lee, C. S. Kim, and B. M. Kim. External line-cavity wavelength-swept source at 850 nm for optical coherence tomography. *IEEE Photon. Technol. Lett.*, 19(3):176–178, 2007. 1041-1135.

[60] R. Huber, M. Wojtkowski, James G. Fujimoto, J. Y. Jiang, and A. E. Cable. Three-dimensional and c-mode oct imaging with a compact, frequency swept laser source at 1300 nm. *Opt. Express*, 13(26):10523–10538, 2005.

[61] R. Huber, M. Wojtkowski, K. Taira, J. Fujimoto, and K. Hsu. Amplified, frequency swept lasers for frequency domain reflectometry and oct imaging: design and scaling principles. *Opt. Express*, 13(9):3513–3528, 2005.

[62] S. M. R. Motaghian Nezam. High-speed polygon-scanner-based wavelength-swept laser source in the telescope-less configurations with application in optical coherence tomography. *Opt. Lett.*, 33(15):1741–1743, 2008.

[63] W. Y. Oh, S. H. Yun, Guillermo J. Tearney, and Brett E. Bouma. 115 khz tuning repitition rate ultrahigh-speed wavelength-swept semiconductor laser. *Opt. Lett.*, 30(23):3159–3161, 2005.

[64] W. Y. Oh, S. H. Yun, B. J. Vakoc, G. J. Tearney, and B. E. Bouma. Ultrahigh-speed optical frequency domain imaging and application to laser ablation monitoring. *Appl. Phys. Lett.*, 88(10):103902–3, 2006.

[65] PH Tomlins and RK Wang. Theory, developments and applications of optical coherence tomography. *Journal of Physics D*, 38:2519–2535, 2005.

[66] Yoshiaki Yasuno, Shuichi Makita, Takashi Endo, Gouki Aoki, Hiroshi Sumimura, Masahide Itoh, and Toyohiko Yatagai. One-shot-phase-shifting fourier domain optical coherence tomography by reference wavefront tilting. *Opt. Express*, 12(25):6184–6191, 2004.

[67] Robert Huber, Desmond C. Adler, and James G. Fujimoto. Buffered fourier domain mode locking: unidirectional swept laser sources for optical coherence tomography imaging at 370,000 lines/s. *Opt. Lett.*, 31(20):2975–2977, 2006.

[68] Yueli Chen, Daniel M. de Bruin, Charles Kerbage, and Johannes F. de Boer. Spectrally balanced detection for optical frequency domain imaging. *Opt. Express*, 15(25):16390–16399, 2007.

[69] H. Lim, J. F. de Boer, B. H. Park, E. C. Lee, R. Yelin, and S. H. Yun. Optical frequency domain imaging with a rapidly swept laser in the 815-870 nm range. *Opt. Express*, 14(13):5937–5944, 2006.

[70] Alan V. Oppenheim and Ronald W. Shafer. *Discrete-Time Signal Processing.* Prentice-Hall, Inc, Upper Saddle River, NJ, 2nd edition, 1999.

[71] S. Yun, G. Tearney, J. de Boer, and B. Bouma. Removing the depth-degeneracy in optical frequency domain imaging with frequency shifting. *Opt. Express*, 12(20):4822–4828, 2004.

[72] Christoph M. Eigenwillig, Benjamin R. Biedermann, Gesa Palte, and Robert Huber. K-space linear fourier domain mode locked laser and applications for optical coherence tomography. *Opt. Express*, 16(12):8916–8937, 2008.

[73] Analog Devices. *Data Conversion Handbook.* Newnes, 2004.

[74] B. Park, Mark C. Pierce, Barry Cense, Seok-Hyun Yun, Mircea Mujat, Guillermo Tearney, Brett Bouma, and Johannes de Boer. Real-time fiber-based multi-functional spectral-domain optical coherence tomography at 1.3 m. *Opt. Express*, 13(11):3931–3944, 2005.

[75] B Vakoc, S Yun, J de Boer, G Tearney, and B Bouma. Phase-resolved optical frequency domain imaging. *Opt. Express*, 13(14):5483–5493, 2005.